Failure of Rock at Low Mean Stress

A THESIS
SUBMITTED TO THE FACULTY OF THE GRADUATE SCHOOL
OF THE UNIVERSITY OF MINNESOTA
BY

Jacob Sharpe

IN PARTIAL FULFILLMENT OF THE REQUIREMENTS
FOR THE DEGREE OF
MASTER OF SCIENCE

Professor Joseph F. Labuz

July 2017

Abstract

Conditions arise in many geoengineering applications where both tensile and compressive normal (effective) stresses act due to change in stress from excavation or pore pressure. However, testing of rock at these stress states associated with low mean stress, say $p < C_0/3$, is rare because of experimental difficulties, where $p = (\sigma_{xx} + \sigma_{yy} + \sigma_{zz})/3$ and Co = uniaxial compressive strength.

The objective of this research is to evaluate rock failure at low mean stress using dog-bone specimens of (dry) Dunnville sandstone. Results from these special triaxial extension tests were used in conjunction with conventional triaxial extension and compression experiments with right-circular cylinders to evaluate four failure criteria: (1) Mohr-Coulomb (*MC*) with a tension cut-off, (2) Paul-Mohr-Coulomb (*PMC*) with a tension cut-off, (3) Hoek-Brown (*HB*), and (4) Fairhurst (*Fh*).

Results for the Dunnville sandstone show that the three failure criteria that either include a tension cut-off (*MC* and *PMC*) or have a "natural" tension cut-off (*Fh*) best capture failure in the low mean stress regime, $-T/3 < p < C_0/3$, where T = uniaxial tensile strength. Of the four criteria considered, *Fh* provided the best overall fit because it is nonlinear and contains a tension cut-off. Fracture surfaces of the dog-bone specimens were evaluated for failure mode based on surface roughness and it was found that there is a transition of decreasing roughness from tensile failure to hybrid (opening and sliding) failure to shear failure.

Table of Contents

List of Tables

List of Figures

Chapter 1: Introduction

1.1 Motivation

Understanding material response to various stress states is of fundamental importance in a number of applications in geoengineering. For example, in the excavation problem of a tunnel or borehole, it is of interest to understand the response of rock, and in particular, to prevent or promote failure. Thus, a greater understanding of rock failure can lead to safer designs and improve constructability.

Failure criteria have been widely studied for rock (Jaeger and Cook 1979). Most work has involved stress states from uniaxial compression to conventional triaxial compression. Even though data obtained for these studies are valuable, testing is needed to characterize failure in the "low" mean stress p regime, defined as

$$p < \frac{C_0}{3} \tag{1}$$

where $p = \dfrac{\sigma_{xx} + \sigma_{yy} + \sigma_{zz}}{3}$ (2)

and C_0 = uniaxial compressive strength (UCS). Stress states at low mean stress can arise near a free surface of an excavation, where with at least one normal stress component is tensile due to a stress concentration. The phenomenon of core discing is an example where failure occurs at low mean stress (Corthésy and Leite 2008). Furthermore, it is well known that an increase of pore pressure in saturated rock can lead to tensile failure (Cornet and Fairhurst 1974).

A criterion such as the popular Mohr-Coulomb is often used to determine the stress state at failure, as depicted in the principal stress plane σ_I-σ_{III} with the compression positive sign convention (Figure 1). The failure surface has slope N and intercept C_0 on the σ_I − axis; the intersection of the failure surface with the hydrostatic axis is denoted V_0, the theoretical triaxial tensile strength. The uniaxial tensile strength T_0 predicted from Mohr-

Coulomb is not measured in experiments and a tension cut-off is often implemented, with very few data to support the approximation beyond the uniaxial stress state. The Mohr-Coulomb failure envelope on a Mohr diagram is shown in Figure 2, where the parameters V_0, T_0, and T are indicated; the intercept on the shear stress axis is c and the slope is *tan ϕ*, where c (cohesion) and ϕ (friction angle) are material parameters related to C_0 and N. The circle with principal stresses $-\sigma_{III} = T$ and $\sigma_I = \sigma_I$* forms the tensile cut-off part of the failure envelope. This thesis involves the development of experimental techniques to evaluate the appropriateness of the tension cut-off and to characterize failure at low mean stress states.
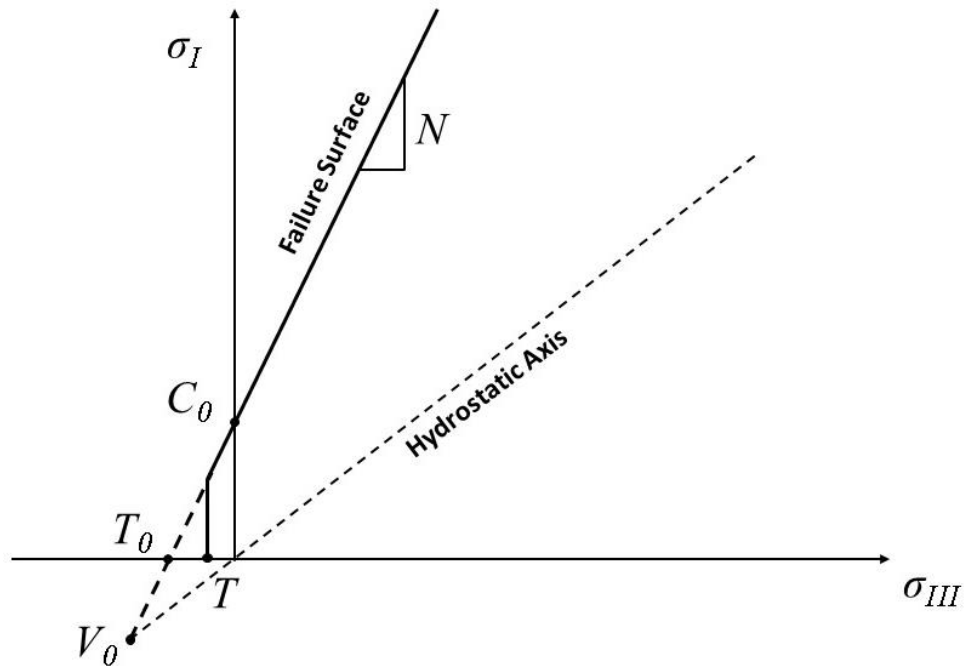
Figure 1. Mohr-Coulomb failure surface with a tension cut-off in the major (σ_I) and minor (σ_{III}) principal stress plane.
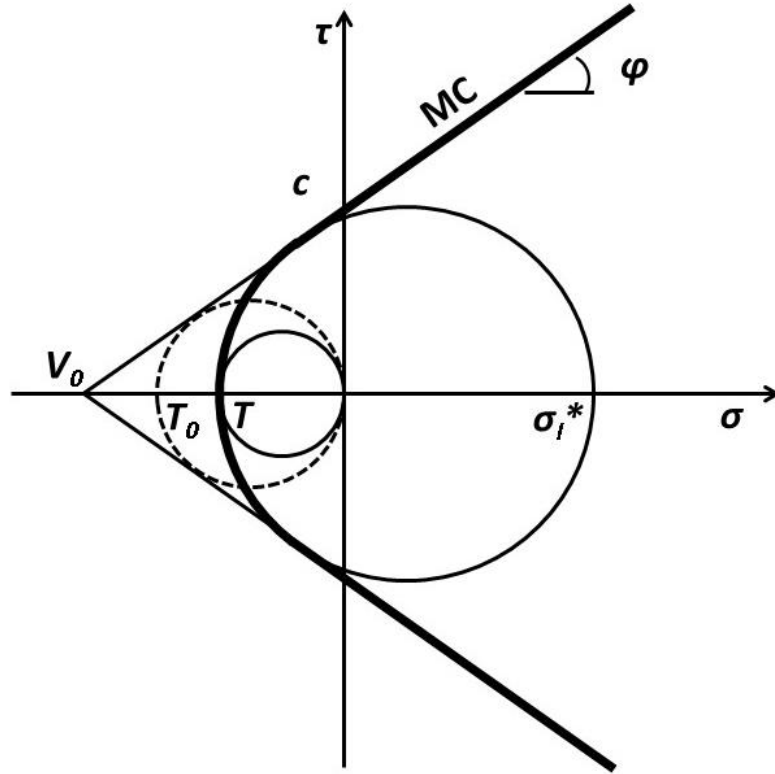
Figure 2. Mohr-Coulomb failure envelope with a tension cut-off (bold) and without a tension cut-off.

1.2 Objective

The main focus of this study is to experimentally investigate failure of rock when the minor principal stress is tensile and the intermediate and major principal stresses are compressive. These tests were conducted using a specific specimen designed in a dog-bone shaped geometry. Various stress regimes were investigated, including low to negative mean stresses, and deformation measurements were recorded. The data in the low mean stress regime with the dog-bone specimen were complimented by results from uniaxial compression, uniaxial tension, conventional triaxial compression, and conventional triaxial extension testing with right circular cylinders. Analysis and comparison of these data with different linear and nonlinear failure criteria were

3

performed. The failure mode of tensile, hybrid, or shear failure and orientation of the failure plane were also analyzed.

1.3 Scope and Organization

This thesis provides experimental data in the low mean stress regime and analyzes how well failure criteria predict the stress state at failure. The thesis is organized into five chapters. Chapter 2 gives a review of stress invariants, background of selected failure criteria, and previous work performed in extension testing in the low mean stress regime. Chapter 3 describes the rock and experimental techniques used in the testing. Chapter 4 analyzes results from extension testing of dog-bone specimens in conjunction with conventional triaxial and uniaxial data. The results are discussed in the context of four failure criteria and observed fracture surfaces. Chapter 5 gives conclusions on the subject matter. Deformation data and other relevant tables and figures are in the Appendices.

Chapter 2: Background

2.1 Stress Invariants

Using a Cartesian coordinate system, the Cauchy stress tensor σ_{ij} gives the state of stress (Figure 3) in terms of normal stresses ($i = j$) and shear stresses ($i \neq j$) acting on an element assuming the sign convention of compression positive:

$$\sigma_{ij} = \begin{bmatrix} \sigma_{xx} & \sigma_{xy} & \sigma_{xz} \\ \sigma_{yx} & \sigma_{yy} & \sigma_{yz} \\ \sigma_{zx} & \sigma_{yz} & \sigma_{zz} \end{bmatrix} \tag{3}$$
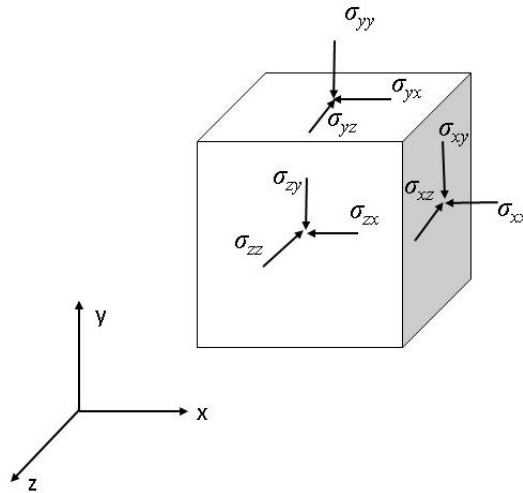
Figure 3. Stress element in Cartesian coordinate system.

For any given state of stress, a coordinate system exists such that no shear stresses act on three perpendicular faces of the element. The three orthogonal axes of this coordinate system (x_I, x_{II}, x_{III}) are the principal axes, and the three corresponding normal stresses are stress invariants called the major σ_I, intermediate σ_{II}, and minor σ_{III} principal stresses ($\sigma_I \geq \sigma_{II} \geq \sigma_{III}$).

$$\sigma_p = \begin{bmatrix} \sigma_I & 0 & 0 \\ 0 & \sigma_{II} & 0 \\ 0 & 0 & \sigma_{III} \end{bmatrix} \qquad\qquad\qquad (4)$$

Note that $\sigma_1, \sigma_2, \sigma_3$ can also represent the principal stresses with no regard to order and six permutations:

$$\sigma_1 \geq \sigma_2 \geq \sigma_3 \qquad\qquad\qquad (5a)$$

$$\sigma_1 \geq \sigma_3 \geq \sigma_2 \qquad\qquad\qquad (5b)$$

$$\sigma_2 \geq \sigma_1 \geq \sigma_3 \qquad\qquad\qquad (5c)$$

$$\sigma_2 \geq \sigma_3 \geq \sigma_1 \qquad\qquad\qquad (5d)$$

$$\sigma_3 \geq \sigma_1 \geq \sigma_2 \qquad\qquad\qquad (5e)$$

$$\sigma_3 \geq \sigma_2 \geq \sigma_1 \qquad\qquad\qquad (5f)$$

This coordinate system is useful when constructing a failure surface, *e.g.* Mohr-Coulomb, where a six-sided pyramid appears, as shown in Figure 4. The plane normal to the hydrostatic axis is called the π-plane, with coordinate axes $\sigma'_1, \sigma'_2, \sigma'_3$.
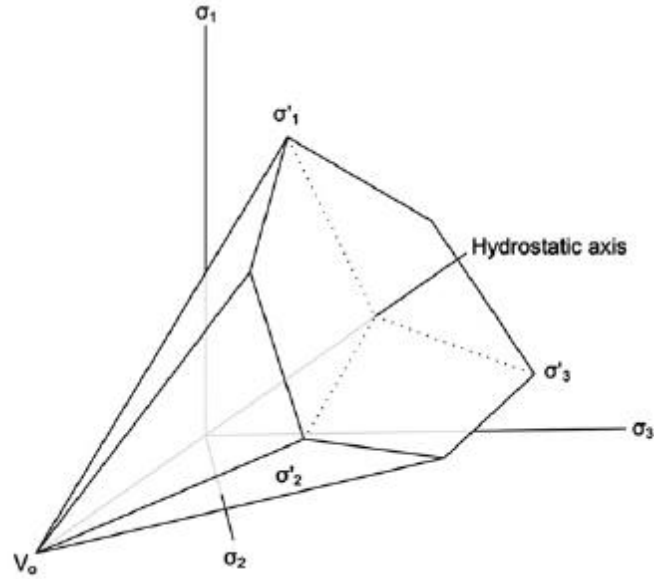
Figure 4. Six-sided pyramidal failure surface in principal stress space σ_1, σ_2, σ_3 with no regard to order (Meyer and Labuz 2013).

Because failure of a material such as rock is often associated with shear stress, it is appropriate to separate the stress tensor into two parts: mean stress (hydrostatic pressure) and deviatoric stress s_{ij}. As defined in Equation 2, mean stress p, where

$$p = \frac{\sigma_{kk}}{3} = \begin{bmatrix} \dfrac{\sigma_1 + \sigma_2 + \sigma_3}{3} & 0 & 0 \\ 0 & \dfrac{\sigma_1 + \sigma_2 + \sigma_3}{3} & 0 \\ 0 & 0 & \dfrac{\sigma_1 + \sigma_2 + \sigma_3}{3} \end{bmatrix} \qquad (6)$$

is related to volume change of the material and for the rock and stress states considered, does not involve failure. Deviatoric stress s_{ij}, where

7

$$
s_{ij} = \sigma_{ij} - p\delta_{ij} = \begin{bmatrix} \dfrac{2\sigma_1 - \sigma_2 - \sigma_3}{3} & 0 & 0 \\ 0 & \dfrac{-\sigma_1 + 2\sigma_2 - \sigma_3}{3} & 0 \\ 0 & 0 & \dfrac{-\sigma_1 - \sigma_2 + 2\sigma_3}{3} \end{bmatrix} \tag{7}
$$

is related to shape change and is typically associated with failure. The shear stress parameter q = deviator stress is introduced:

$$
q = \sqrt{\frac{3}{2} s_{ij} s_{ji}} = \sqrt{\frac{1}{2}\left[(\sigma_1 - \sigma_2)^2 + (\sigma_2 - \sigma_3)^2 + (\sigma_3 - \sigma_1)^2\right]} \tag{8}
$$

For axisymmetric conditions of conventional triaxial testing, it is convenient to express the stress state in terms of axial stress σ_a and radial stress σ_r, which is sometimes referred to as confining pressure. For loading of a right, circular cylinder (Figure 5), the principal stresses are

$$
\sigma_a = \sigma_1 \tag{9}
$$

$$
\sigma_r = \sigma_2 = \sigma_3 \tag{10}
$$
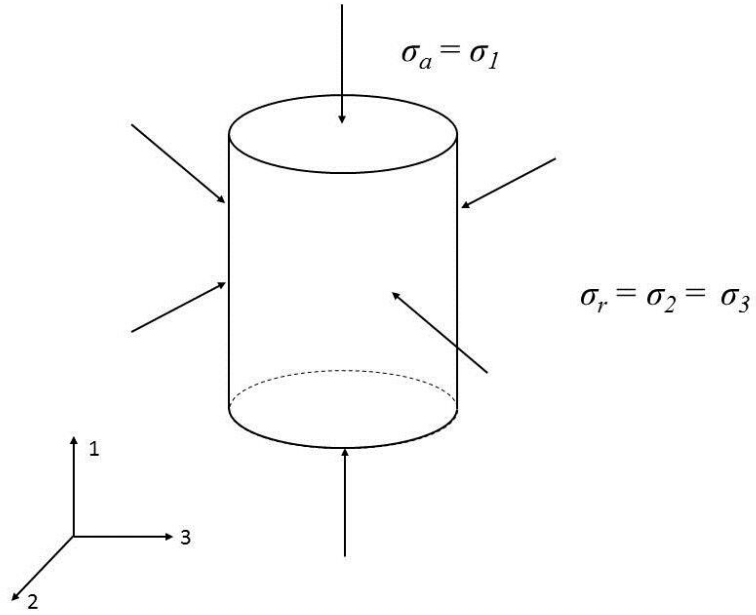
Figure 5. Axisymmetric stress state in conventional triaxial testing.

For the case of axisymmetric loading, q reduces to

$$q = \sqrt{\frac{1}{2}\left[\left(\sigma_a - \sigma_r\right)^2 + \left(\sigma_r - \sigma_a\right)^2\right]} \qquad (11)$$

and

$$q = \sigma_a - \sigma_r \qquad (12)$$

By convention, $q > 0$ is associated with compression and $q < 0$ is extension. The mean stress is

$$p = \frac{\sigma_a + 2\sigma_r}{3} \qquad (13)$$

2.2 Failure Criteria

Failure of rock and other geomaterials has been a topic of concern dating back to the classic experiments of Von Karman (1911). Over the years, numerous studies have been conducted to describe failure under various stress states and statistical analyses and fitting methods have been applied (Murrell 1965; Carter *et al*. 1991; Pincus 2000; Pariseau 2007).

The simplest failure criterion for geomaterials was proposed by Coulomb (1776) in an effort to analyze retaining walls. Failure occurs when the shear stress τ on a plane is equal to the sum of a pressure-dependent component produced by the normal stress σ on the plane multiplied by a material constant (*tan ϕ*) and a cohesive component (*c*) that is another material constant:

$$|\tau| = c + \sigma \tan \varphi \tag{14}$$

where c = cohesion and ϕ = angle of internal friction. Coulomb's criterion takes on a linear form on a Mohr diagram.

Mohr (1900) defined a failure criterion that is characterized by a group of Mohr circles described by principal stresses. The family of Mohr circles forms an envelope, where the normal and shear stresses at failure are found by the tangency of the envelope to the Mohr circles (Figure 6). Mohr's criterion can be linear or nonlinear.
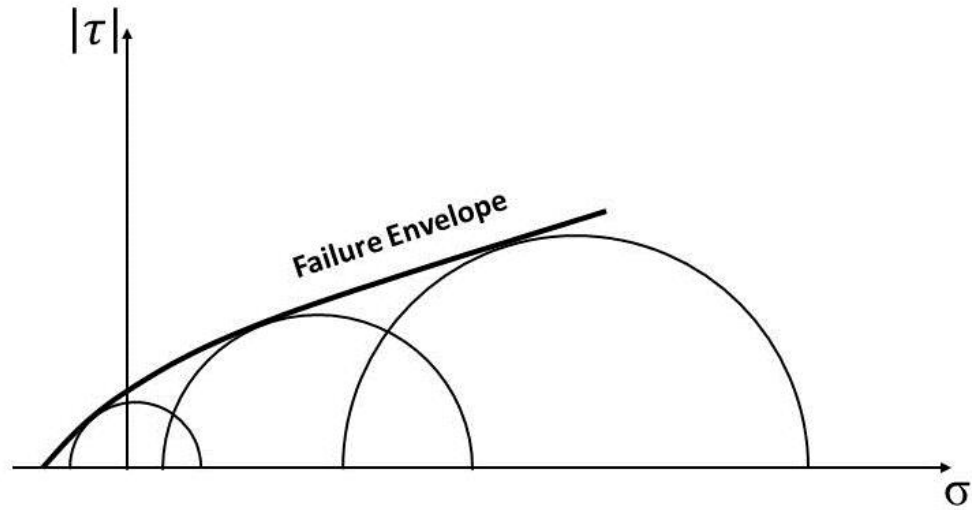
Figure 6. Family of Mohr circles with corresponding failure envelope.

Mohr-Coulomb

A combination of Mohr's and Coulomb's theories (Nadai 1950) has been widely used. The Mohr-Coulomb failure criterion (MC) is a linear failure envelope that is a best fitted line such that the failure envelope is tangent to the Mohr circles. The failure criterion can be written in terms of the major and minor principal stresses, a parameter N, and the uniaxial compressive strength C_0:

$$\sigma_I = N\sigma_{III} + C_0 \tag{15}$$

$$N = \frac{1 + \sin\varphi}{1 - \sin\varphi} \tag{16}$$

Note that there is no dependence of the intermediate principal stress. The Mohr-Coulomb criterion is popular, as the friction angle and uniaxial compressive strength can be determined with a few lab tests. Mohr-Coulomb has been shown to be a reasonable approximation for a limited range of confining stresses, as typical failure envelopes become nonlinear with increasing confining stress (Tarokh *et al*. 2016).

11

Another drawback of Mohr-Coulomb is the overestimation of the uniaxial tensile strength, often times by greater than an order of magnitude. Paul (1960) suggested including a tension cut-off to improve the accuracy of the prediction, as shown in Figure 1 and described by

$$\sigma_I = N\sigma_{III} + C_0 \text{ for } \sigma_I > \sigma_I^* \tag{17}$$

$$-\sigma_{III} = T \text{ for } \sigma_I \le \sigma_I^* \tag{18}$$

$$\text{where } \sigma_I^* = C_0 - NT \tag{19}$$

It is also convenient to express a failure criterion in terms of mean stress p, deviator stress q, and Lode angle θ (Figure 7). Using an approach from Nayak and Zienkiewicz (1972), the principal stresses can be written in terms of p, q, and θ:

$$\sigma_1 = p + \frac{2}{3}q\cos\theta \tag{20}$$

$$\sigma_2 = p - \frac{2}{3}q\sin\left(\frac{\pi}{6} + \theta\right) \tag{21}$$

$$\sigma_3 = p - \frac{2}{3}q\sin\left(\frac{\pi}{6} - \theta\right) \tag{22}$$

where the Lode angle θ is related to the stress path. For conventional triaxial compression $\theta = 0°$, and for extension, $\theta = 60°$. Mohr-Coulomb can be expressed in the p-q plane with a tension cut-off for the case of conventional triaxial compression $\theta = 0°$:

$$p + \frac{2}{3}q = N\left(p - \frac{1}{3}q\right) + C_0 \tag{23}$$

$$q = \frac{3[C_0 + p(N-1)]}{N+2} \text{ for } p > p^* \tag{24}$$

$$q = T_0(N-1) + C_0 \text{ for } V_0 \le p \le p^* \tag{25}$$

The case of conventional triaxial extension $\theta = 60°$.

$$q = \frac{3[-C_0 + p(1-N)]}{2N+1} \qquad (26)$$

Recall that V_0 represents the vertex that is associated with uniform triaxial tension. Using a tension cut-off provides an accurate representation of the tensile strength, but it is unclear how well it "works" in the low mean stress regime. Of course, the tension cut-off makes a third parameter needed to describe the failure surface, or an assumption needs to be made on the ratio between uniaxial compressive to uniaxial tensile strengths n:

$$n = \frac{C_0}{T} \qquad (27)$$
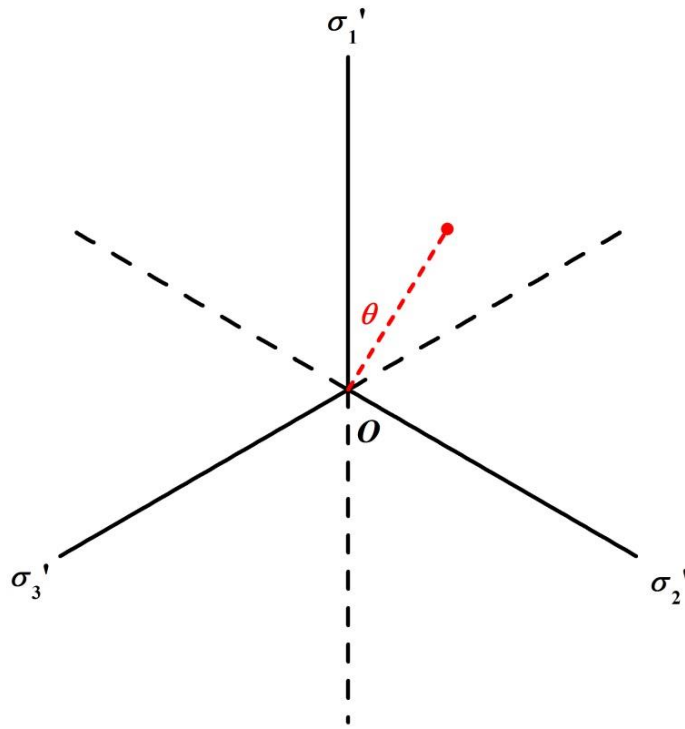
Figure 7. Representation of π-plane and transformation from principal stresses to p-q-θ.

Paul-Mohr-Coulomb

Meyer and Labuz (2013), based on the work of Paul (1968), proposed a variation of the classical Mohr-Coulomb criterion that accounts for the intermediate principal stress, so-called Paul-Mohr-Coulomb (PMC). It requires three parameters: friction angle in compression φ_c, friction angle in extension φ_e, and the uniform triaxial tensile strength V_0:

$$\frac{\sigma_I}{V_0} N_c - \frac{\sigma_{II}}{V_0}\left(N_c - N_e\right) - \frac{\sigma_{III}}{V_0}\left(N_e + 1\right) = 1 \tag{28}$$

$$N_c = \frac{1 - \sin\varphi_c}{2\sin\varphi_c} \tag{29}$$

$$N_e = \frac{1 - \sin\varphi_e}{2\sin\varphi_e} \tag{30}$$

PMC can be represented in the p-q plane by

$$q = \frac{b_\theta}{V_0} p + b_\theta = b_\theta\left(\frac{p}{V_0} + 1\right) \tag{31}$$

where b_θ is the intercept with the q-axis of a particular (θ = constant) multi-axial failure surface and $b_e \leq b_\theta \leq b_c$. For the case of compression $b_\theta = b_c$ and for extension $b_\theta = b_e$.

Similar to Mohr Coulomb, Paul-Mohr-Coulomb overestimates the uniaxial tensile strength. It is suggested to incorporate a tension cut-off also with PMC by either knowing the uniaxial tensile strength or again assuming a value of the ratio n. From Figure 8, it should be noted that the tension cut-off for the compression surface predicts failure under biaxial tension, where $\sigma_I = 0$, $\sigma_{II} = \sigma_{III} = -T$.
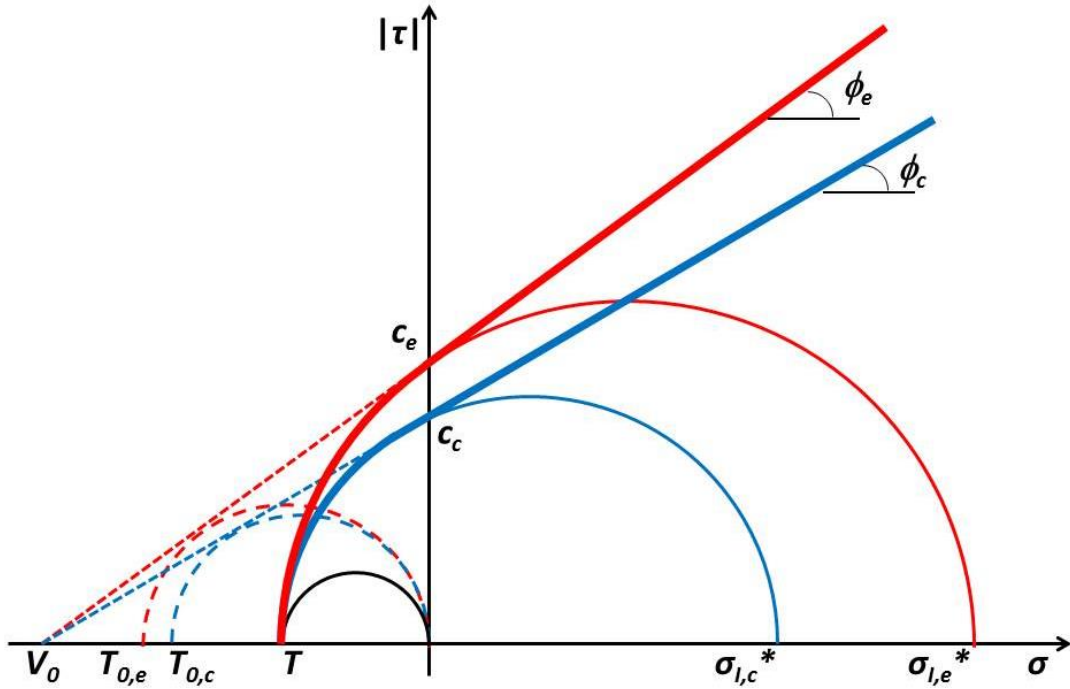
Figure 8. Paul-Mohr-Coulomb failure envelopes in compression (blue) and extension (red) with a tension cut-off (bold) and without a tension cut-off (dashed).

Hoek-Brown

Since many researchers have discovered that the failure envelope for most rock is nonlinear over a larger range of mean stresses, Hoek and Brown (1980) proposed a criterion in terms of principal stresses that takes the form of a square-root function:

$$\sigma_I = \sigma_{III} + C_0 \sqrt{m_b \frac{\sigma_{III}}{C_0} + 1} \tag{32}$$

Hoek and Brown developed the criterion with a fitting parameter m_b and the uniaxial compressive strength C_0. The HB criterion has been widely adopted by the rock mechanics community and many parameter generalizations and adaptations have been

15

proposed (Hoek *et al.* 2002) for rock masses (Hoek and Brown 1988) or for relating the criterion's parameters to typical Mohr-Coulomb parameters (Hoek 1990; Hoek 1994). Hoek-Brown can also be expressed in the *p-q* plane by the transformation equations (20-22):

$$p + \frac{2}{3}q = p - \frac{1}{3}q + C_0 \sqrt{m_b \frac{p - \frac{1}{3}q}{C_0} + 1} \tag{33}$$

and simplifying we get

$$q = \frac{1}{6}\left(\sqrt{C_0} \sqrt{C_0 m_b^2 + 36C_0 + 36 m_b p} - C_0 m_b \right) \tag{341}$$

Hoek-Brown typically performs better than Mohr-Coulomb over a wide range of confining stresses. However, some have noted that a tension cut-off is still needed for HB (Hoek and Martin 2014). Although others have expressed a generalized Hoek-Brown in a Mohr diagram (Hoek 1983), an unappealing feature is that the criterion is discontinuous in the Mohr plane in the transition from positive to negative shear stress (Pariseau 2007), whereas the Fairhurst (1964) failure criterion is continuous (Figure 9).
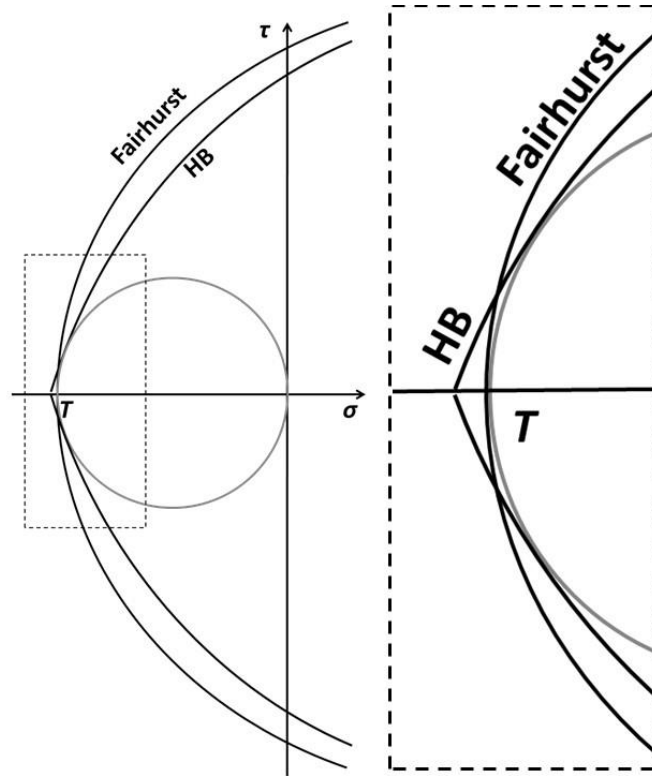
Figure 9. Comparison of Hoek Brown and Fairhurst criteria near the Mohr circle of uniaxial tension.

Fairhurst

Fairhurst (1964) developed a failure criterion in his effort to better understand failure in tensile testing for rock. The Griffith fracture criterion can be represented as a parabola in a Mohr diagram:

$$\tau^2 = 4T\,(T - \sigma) \tag{35}$$

Griffith's theory is based on the predicted ratio of $n=8$, which is typically not observed for rock. Fairhurst decided to generalize the criterion for an arbitrary ratio n. The parameters for the criterion are the uniaxial tensile (T) and compressive (C_0) strengths or it can also be expressed in terms of their ratio (n):

$$\tau^2 = (m-1)^2 T(T - \sigma) \tag{36}$$

$$m = \sqrt{n+1} \tag{37}$$

When the transformation is performed to principal stress plane, the failure criterion has a natural tension cut-off (Figure 10):

$$\sigma_{III} = T \text{ for } \sigma_I \leq -T\, m(m-2) \tag{38}$$

$$\frac{(\sigma_I - \sigma_{III})^2}{\sigma_I + \sigma_{III}} = -2(m-1)^2 T \left[1 + \frac{2T}{\sigma_I + \sigma_{III}} \left\{ \left(\frac{m-1}{2} \right)^2 - 1 \right\} \right] \text{ for} \tag{39}$$

$$\sigma_I > -T_0 m(m-2)$$

$$\sigma_I = \sigma_{III} - T + 2Tm + 2m \left[T\left(T - \sigma_{III} \right) \right]^{\frac{1}{2}} - Tm^2 - 2 \left[T(T - \sigma_{III}) \right]^{\frac{1}{2}} \text{ for} \tag{40}$$

$$\sigma_I > -Tm(m-2)$$

The criterion is not commonly used in practice, but others who have analyzed low mean stress failure data have suggested a parabolic failure criterion, and Hoek and Martin (2014) have also mentioned the use of the Fairhurst criterion.
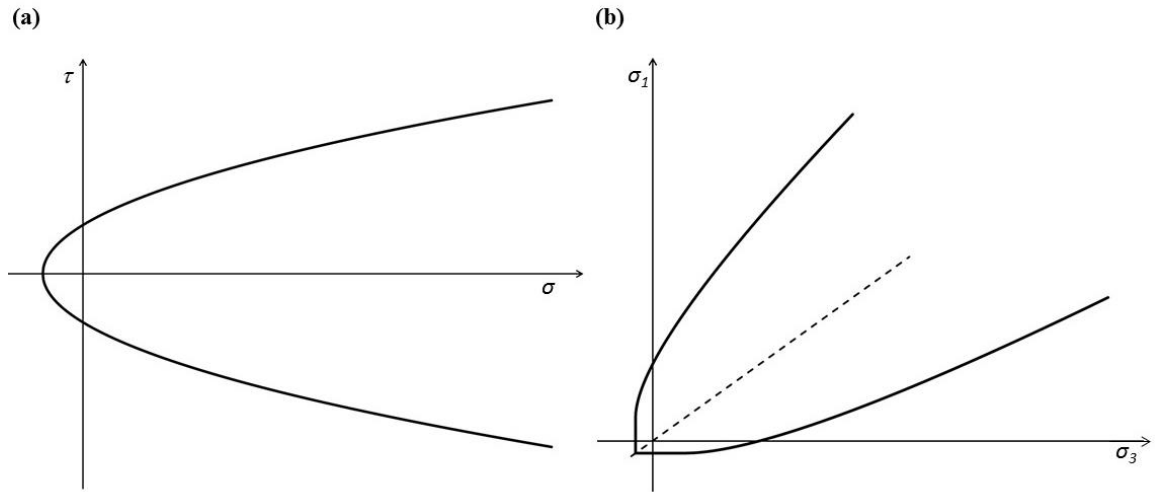
Figure 10. (a) Fairhurst parabola in the Mohr plane and (b) principal stress plane.

2.3 Failure at Low Mean Stress

Brace (1964) was one of the earliest researchers to gather significant failure data at low mean stresses by performing triaxial extension tests using dog-bone specimens of Blair and Webatuck dolomites, Chershire quartzite, Westerly granite, and Frederick diabase. All the rocks tested have uniaxial compressive strengths that range from 230 MPa to over 500 MPa, very strong rock.

Motivated by the work of Voigt (1899) and Bridgman (1937), Brace used dog-bone shaped specimens to perform triaxial testing at low mean stresses. The confining pressure and geometry of the specimen, specifically the change in cross-sectional area, generates a force in the axial direction and can produce a net tensile force (Figure 11). However, difficulty was had in sealing (jacketing) the specimens, as Brace used various metal jackets. Results from the study included monotonically increasing fracture inclination from normal to the axial stress ($\theta = 0$ for tension failure) to $\theta = 45 + \varphi/2$ for shear failure. He also observed a steeper slope of the failure surface at low mean stress than higher mean stress.

$$P_c = \sigma_r$$

$$\sigma_a = \frac{F - \sigma_r (A_o - A_i)}{A_i}$$

$$F > \sigma_r (A_o - A_i) \rightarrow \sigma_a = Compressive$$
$$F < \sigma_r (A_o - A_i) \rightarrow \sigma_a = Tensile$$
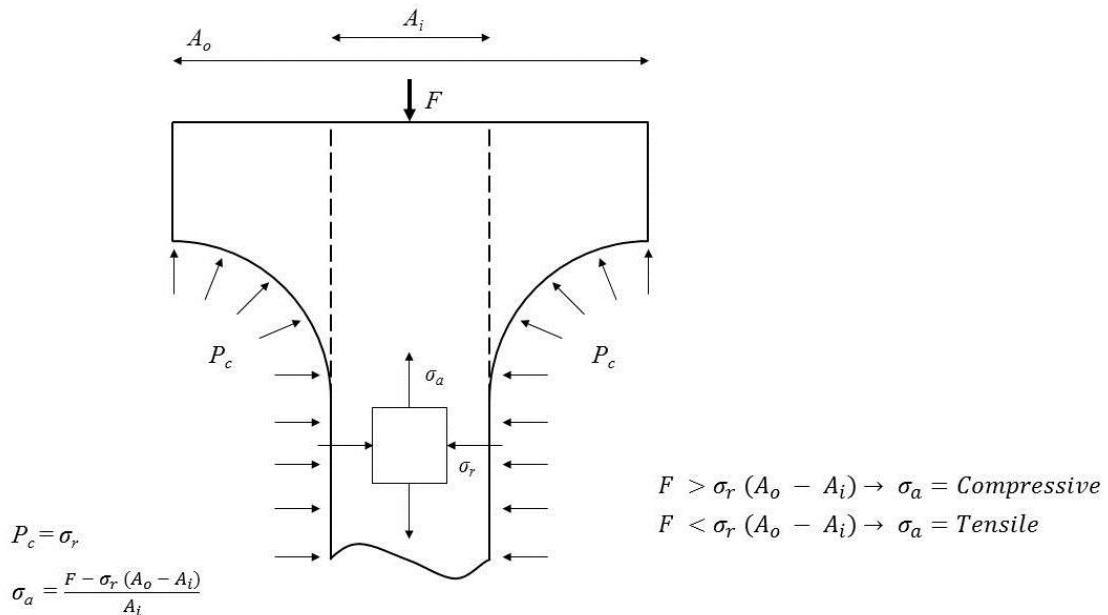
Figure 11. Effect of differential area on axial stress for a dog-bone geometry specimen.

Ramsey and Chester (2004) used a similar idea to Brace of a dog-bone geometry to produce failure at low mean stresses for Carrara marble. A large radius was used to create the area difference in the throat region of the specimens but this resulted in a continuous variation of the cross-sectional area. Jacketing was accomplished by using clay to fill the empty space of the dog-bone specimen to create a pseudo right cylindrical specimen.

Results were focused on the transition of fracture surfaces from tensile opening to hybrid (opening and sliding) to shear sliding. Failure data under very low mean stresses showed that the minor principal stress was near the uniaxial tensile strength.

Others have performed similar testing (Schock and Louis 1982) or some variation like tension testing under confining pressure (You 2010) or confined Brazilian testing (Jaeger and Hoskins 1966). A Griffith type criterion (Griffith, 1924) for tensile failure reasonably agreed with the experiments (Brace, 1964; Jaeger and Hoskins 1966; Schock and Louis 1982; Ramsey and Chester 2004). Traditional failure criteria were not evaluated in the low mean stress regime.

Chapter 3: Experimental Techniques

3.1 Rock Properties

Dunnville sandstone from central Wisconsin was selected for experimental investigation. It is composed of roughly 95 percent quartz grains and little cementitious materials making it a quartz arenite. The rock is light brown to tan in color and the bedding is observable. Measurements of porosity, density, P-wave velocity, and S-wave velocity on the tested blocks yielded results of 30%, 1.800 ± 0.011 g/cm^3, 1971 ± 65 m/s, and 1056 ± 30 m/s respectively (averages and standard deviations). P-wave and S-wave velocity measurements were taken normal to bedding (1930 ± 21 m/s, 1045 ± 28 m/s) and in two orthogonal directions parallel to bedding (2012 ± 63 m/s, 1075 ± 16 m/s), and the results showed little variation. For this reason, the tested rock is assumed to be isotropic and homogeneous.

Figure 12. Photo of Dunnville sandstone.

A diamond tipped core barrel and saw blade, along with a tungsten carbide surface grinder, were used to fabricate right cylindrical specimens. Length to diameter ratios ranged from 1.9 – 2.7, depending on the type of test being performed.

3.2 Uniaxial Compression and Tension

Uniaxial compression and tension tests were conducted to determine elastic and strength parameters. Two right cylindrical specimens were loaded under uniaxial compression and brought to failure while also measuring axial and radial strain by extensometers. These tests provided values of uniaxial compressive strength C_o, Young's modulus E, and Poisson's ratio ν (Figure 13). Other specimens that were instrumented with strain gages were also used to evaluate Young's modulus and Poisson's ratio, but were not brought to failure. Results are presented in Table 1.

An estimate of uniaxial tensile strength was gathered via Brazilian tests on 50 mm diameter disks that were roughly 25 mm in thickness. Brazilian tests typically give over estimates of tensile strengths (Goodman 1989), so direct tensile tests were performed on thin (6 mm thick) coupon samples similar to those used for tensile testing of metals. Friction grips were used to grab the wider head area of the specimen and failure developed in the thinner throat region. A clip gage was attached to the throat region to measure axial strain in tension (Figure 14).

Table 1. Measured strength and elastic parameters in compression and tension.

Loading	Uniaxial Strength [MPa]	ν [-]	E [GPa]	K [GPa]
Compression	29.3±0.6	0.31±0.02	8.2±0.2	8.9±0.3
Loading	Uniaxial Strength [MPa]	Brazilian [MPa]	E [GPa]	
Tension	1.0±0.1	2.0±0.1	2.3±0.5	

(a)

(b)
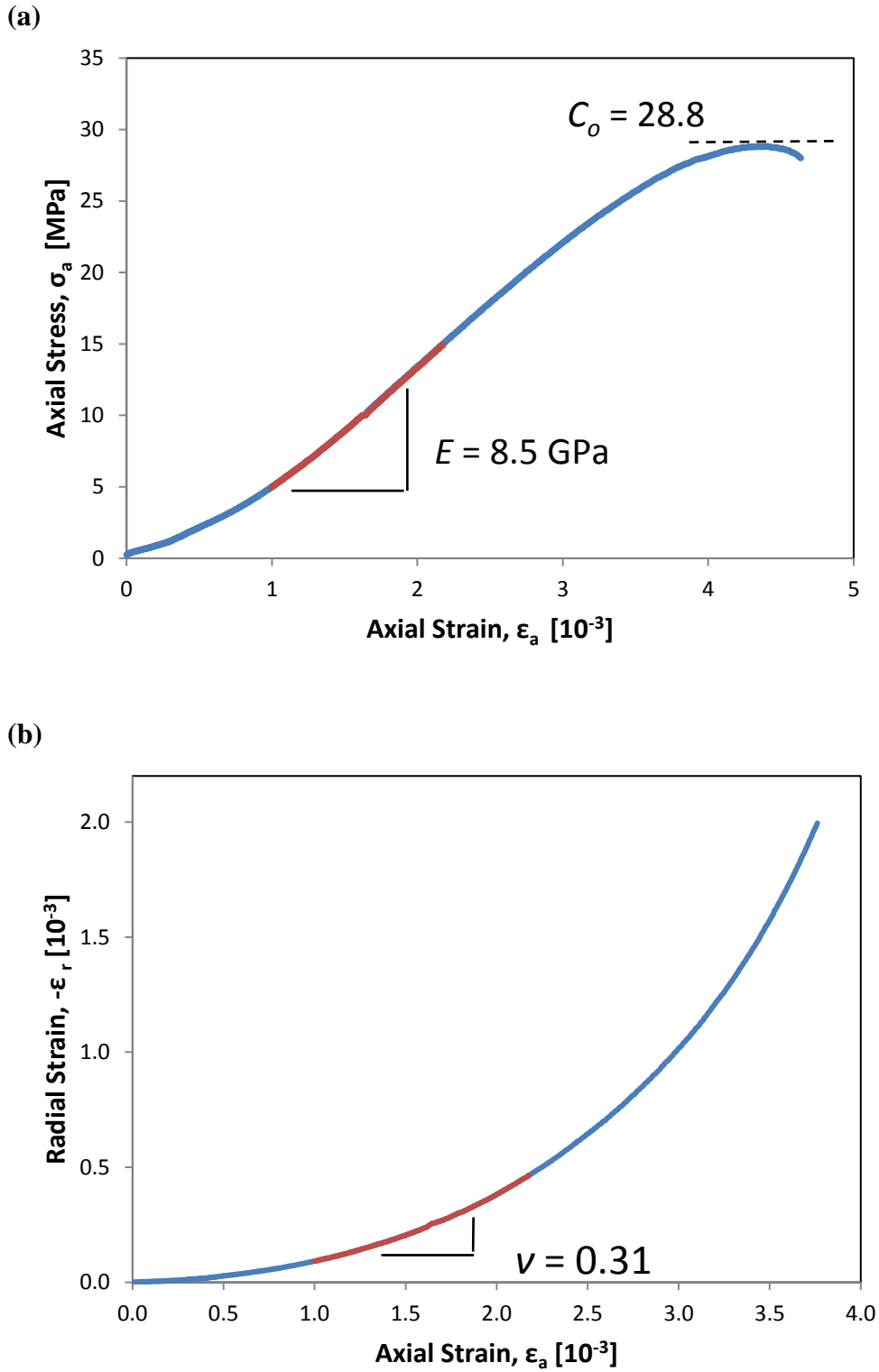
Figure 13. Uniaxial compression of Dunnville sandstone. (a) Axial stress-axial strain response. (b) Radial strain-axial strain response.
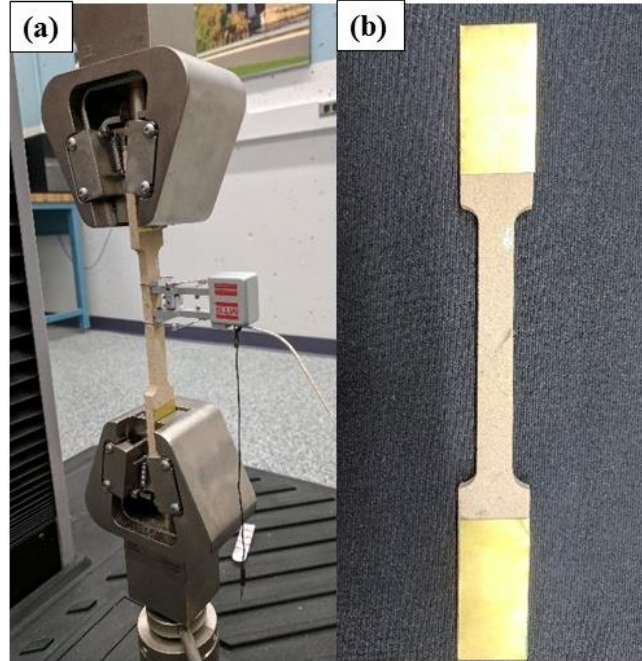
Figure 14. (a) Experimental setup for direct tension testing and (b) coupon specimen.

3.3 Conventional Triaxial Compression and Extension

Conventional triaxial tests were performed to determine the shear strength of Dunnville sandstone. Two different stress paths of triaxial compression ($q > 0$) and triaxial extension ($q < 0$) were used.

Conventional triaxial compression tests are performed in a pressure vessel with confining fluid pressure p_c used to apply the radial stress σ_r, and an axial (deviatoric) force F_D, is applied with an actuator.

$$\sigma_a = \frac{F_D}{A} + \sigma_r \tag{21}$$

A Hoek-Franklin cell is convenient for extension testing because the axial stress and radial stress are applied independently. The Hoek-Franklin cell uses a specially designed rubber membrane to isolate the specimen from the confining fluid and seal the pressure

vessel. Since the confining fluid is isolated from the specimen and loading platens, it does not act in the axial direction; this allows for extension tests to be performed easily with the cell. The axial stress is

$$\sigma_a = \frac{F}{A} \tag{42}$$

Stearic acid was used to reduce friction between the specimen and loading platens (Labuz and Bridell 1993). The specimen diameter was nominally 30 mm and the length ranged from 65 – 83 mm. Compression tests were performed by triaxial compression loading. A hydrostatic stress state was developed by applying equal axial and radial stresses, then axial stress was increased by a specific axial displacement rate until failure, identified by a maximum deviator stress. Figure 15 shows triaxial compression specimens failed at various confining pressures using the Hoek-Franklin cell. Extension tests were performed by triaxial extension unloading. A hydrostatic stress state was developed and then axial stress was decreased by a specified axial displacement rate until failure, identified by a minimum deviator stress (Figure 16).

Figure 15. Shear failure of triaxial compression specimens at radial stresses of 2.5 (left), 5, 10, 20 and 30 (right) MPa.
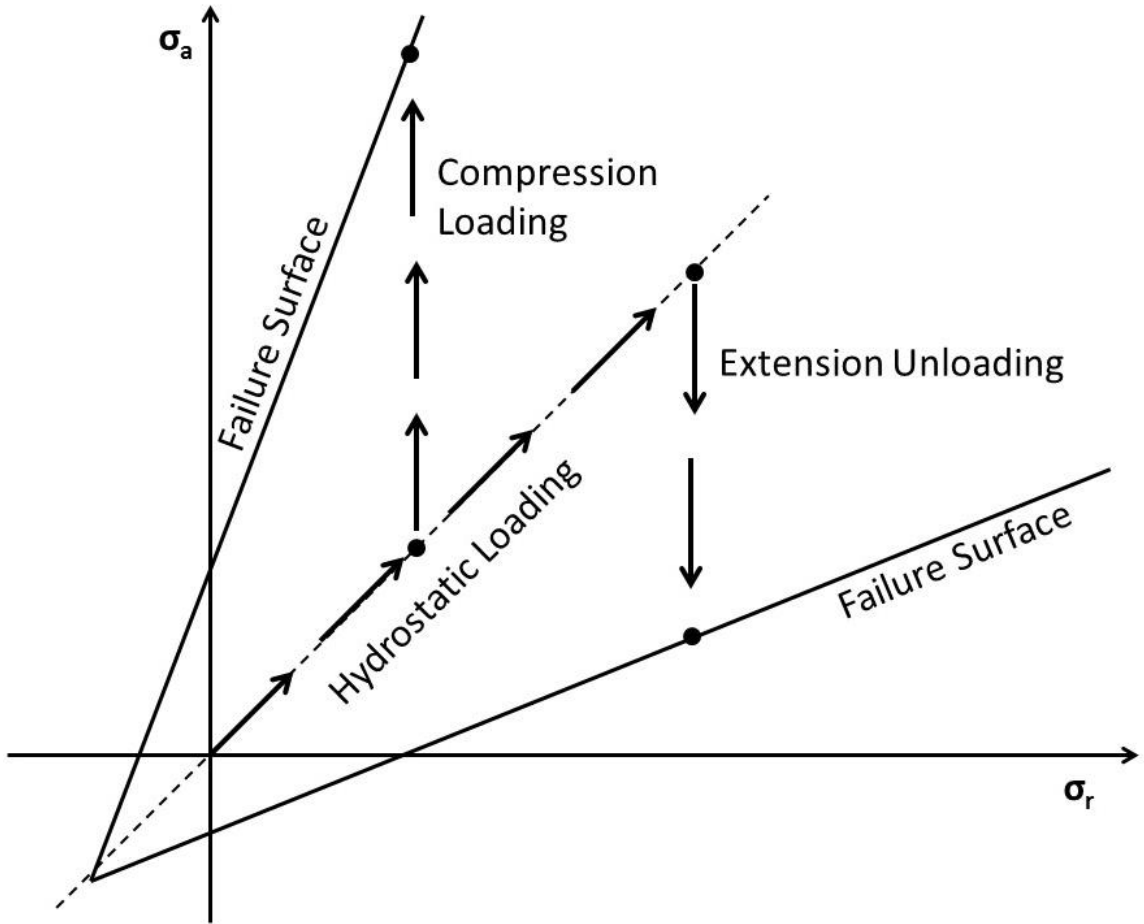
Figure 16. Stress path for triaxial compression loading and triaxial extension unloading.

3.4 Dog-bone Triaxial Extension

The axisymmetric dog-bone specimen was chosen as the geometry to generate tensile stress over a portion of the rock, similar to Brace (1964). By this design, the major principal stress was applied radially while the minor principal stress was developed in the axial direction. This results in a triaxial extension test.
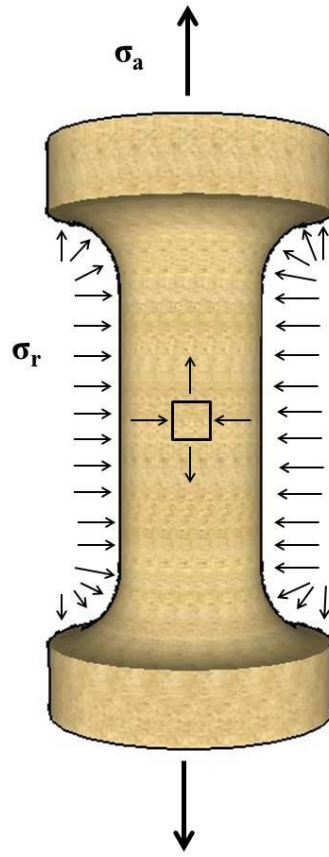
Figure 17. Dog-bone specimen.

The axial stress of a dog-bone specimen can be expressed as a sum of two forces over the cross-sectional area of the throat, A_i:

$$\sigma_a = \frac{F_1 + F_2}{A_i} \tag{43}$$

where F_1 is the mechanical force applied by the actuator and F_2 is the force generated by the confining pressure acting over the differential area of the dog-bone specimen. This force acts in tension over the throat cross-sectional area:

$$F_2 = -\sigma_r (A_o - A_i) \tag{44}$$

Equation (43) can then be expressed as

$$\sigma_a = \frac{F_1 - \sigma_r(A_o - A_i)}{A_i} \tag{45}$$

The mechanical force F_1 needed to achieve a hydrostatic stress state in the throat region of the dog-bone specimen can be solved for a known geometry by setting the axial and radial stresses equal:

$$\sigma_a = \sigma_r = \frac{F_1 - \sigma_r(A_o - A_i)}{A_i} \tag{46}$$

$$F_1 = \sigma_r(A_o - A_i) + \sigma_r A_i \tag{47}$$

$$F_1 = \sigma_r A_o \tag{48}$$

To achieve an extensional stress state, the axial stress must be less than the radial stress, which can be written in terms of the applied mechanical force F_1:

$$F_1 < \sigma_r A_o \tag{49}$$

The mechanical force needed to have an axial stress less than or equal to zero can be determined by setting Equation 43 equal to zero:

$$0 = \frac{F_1 - \sigma_r(A_o - A_i)}{A_i} \tag{50}$$

$$F_1 \leq \sigma_r(A_o - A_i) \tag{51}$$

3.5 Dog-bone Geometry

Rock samples were first cored using a traditional diamond-tipped core barrel to produce right circular cylinders. A computer numerically controlled (CNC) lathe was used to precisely machine the specified dog-bone specimen with dimensions shown in Figure 18.
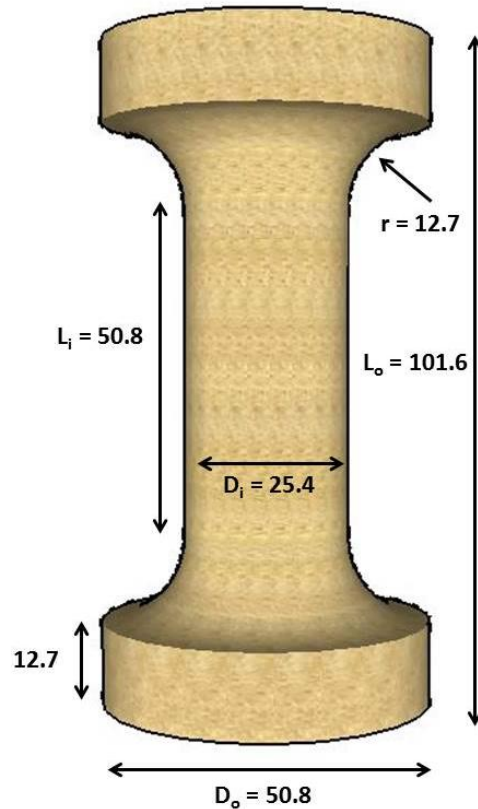
Figure 18. Dog-bone specimen dimensions. Subscript "i" denotes throat region, subscript "o" denotes head region. Dimensions in mm.

The specific dog-bone design was selected with two primary factors in mind. The first was the desire for a uniform state of stress in the throat of the specimen. The throat is a 2:1 length to diameter ratio, similar to a typical cylindrical specimen. The issue of a stress concentrator arises due to the radius to create the dog-bone shape. This impacts the stress near the boundary of the throat region, but if the length is large enough, there will be a region of uniform stress in the throat. Indeed, results from an elastic stress analysis show this to be the case (Figure 19a), and the state of stress is more or less the same through 50% of the throat length (L_i).

The stress analysis in Figure 19a also illustrates that the region of highest stress is located near the radius ($r = 12.7$ mm), in the transition between the throat and the head. The

stress concentration factor (SCF) is 1.1, which was judged to be adequate in allowing failure to develop in the uniform stress region. Other researchers have used a specimen of large radius (r = 91 mm), shown in Figure 19b, which features a continuous variation in cross-sectional area. This specimen design reduces the SCF but a region of uniform stress does not exist along the axis (Figure 19b). For tensile failure, where the fracture plane develops normal to the minor principal stress, the change in stress state along the axial direction is not an issue. For hybrid failure, where the fracture plane is oblique to the minor principal stress, the state of stress varies considerably.

Figure 20 shows the axial stress at two sections, one at mid-length ($L_i/2$) and one at 20% of $L_i/2$, for the two different geometries. Obviously, because of the varying cross-sectional area, the axial stress varies along the throat of the specimen. For the design used in this study, where the cross-section is constant over the length L_i, the stress distribution does not vary due to location of the profile and the deviation in axial stress along the throat length is less than one percent.
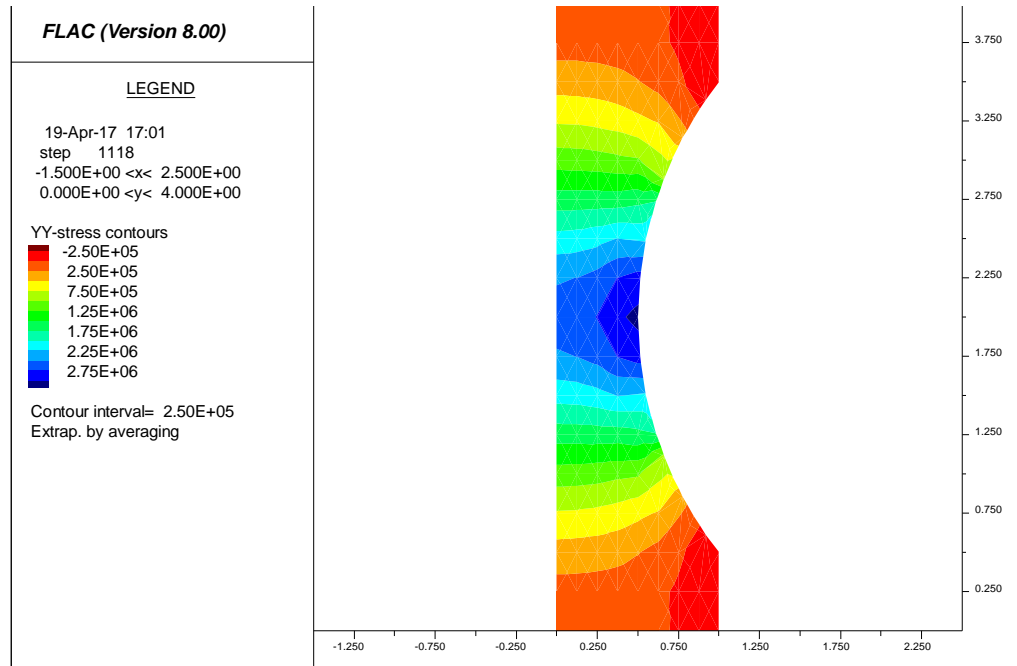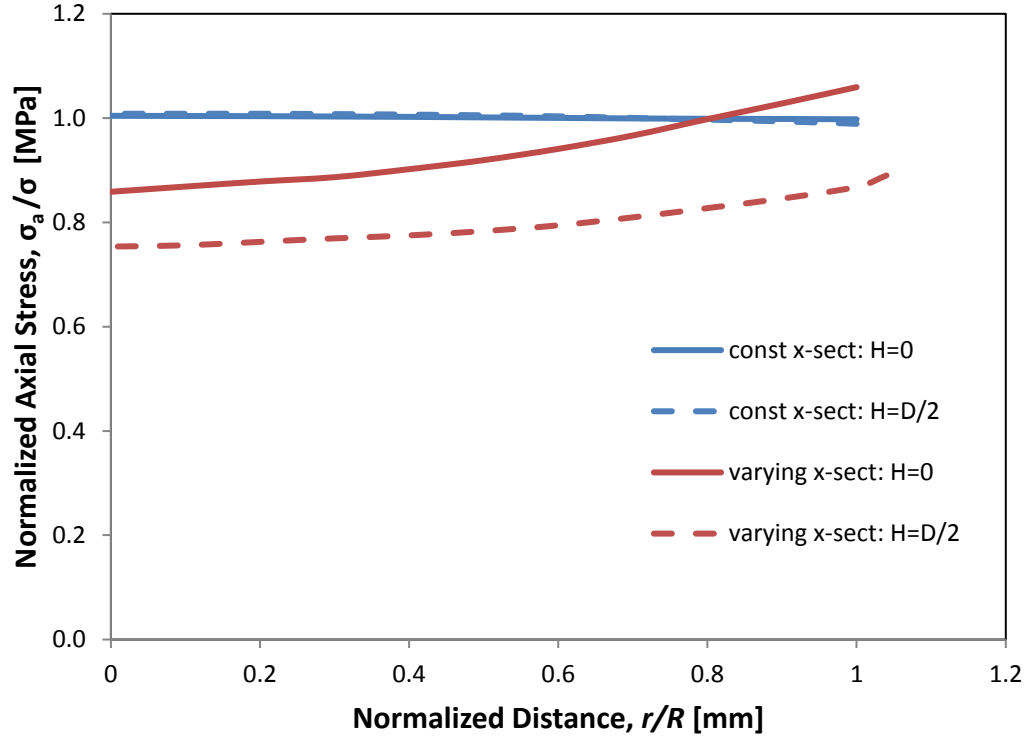
(a)
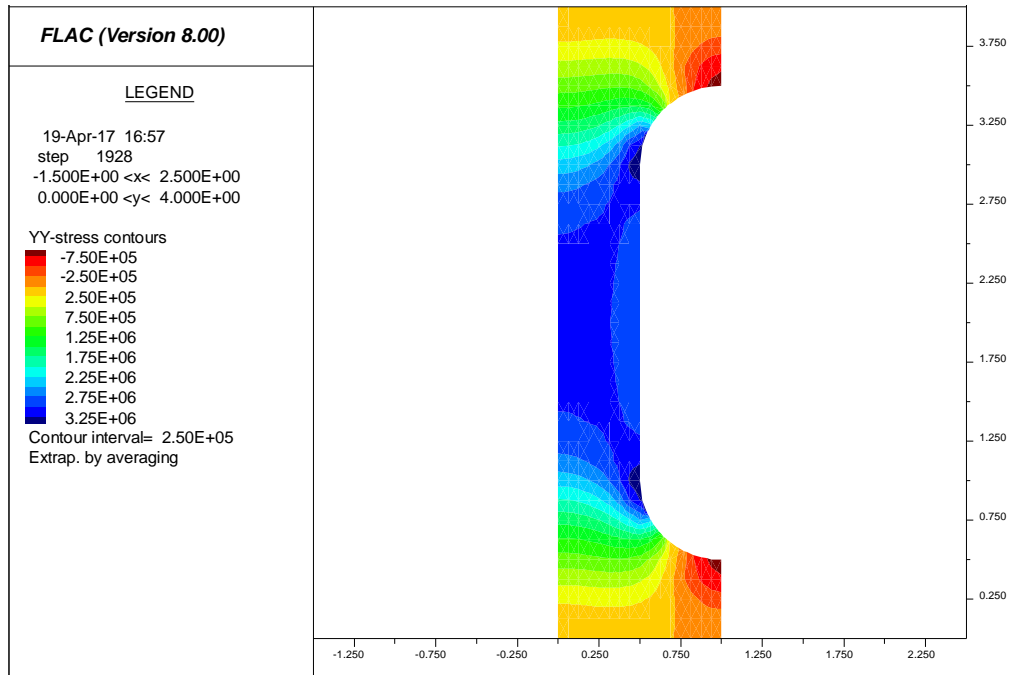
(b)

Figure 19. Elastic stress analysis in axial direction using FLAC for dog-bone specimen geometry with (a) uniform throat region and (b) without uniform throat region.

(a)

(b)
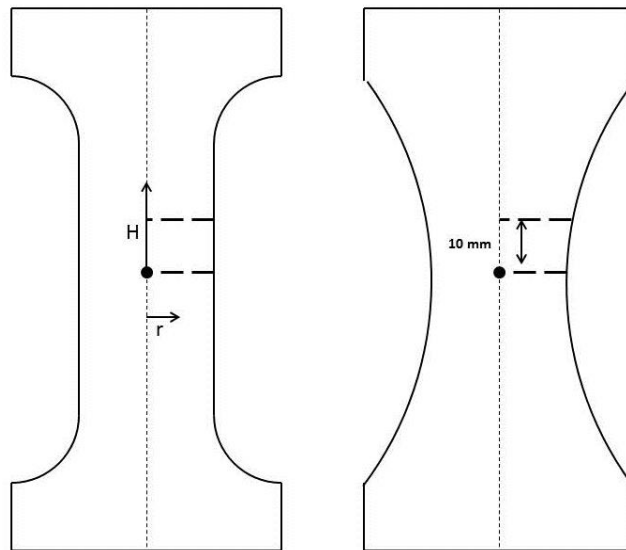
Figure 20. (a) Profiles of axial stress distribution across radius of uniform and non-uniform dog-bone specimens. (b) Locations of profiles (bold, dashed) for both dog-bone specimens.

The second factor for the specific dimensions was the minimum mean stress. One objective was to perform a test where the specimen was under zero or negative mean stress at failure. A state of stress where mean stress is zero is the special case of pure shear.

$$p = 0 \rightarrow \sigma_a = -2\sigma_r \qquad (52)$$

The axial stress can be rewritten in the form

$$\frac{F}{A_i} - \frac{\sigma_r(A_o - A_i)}{A_i} = -2\sigma_r \qquad (53)$$

The force can be set to zero, which eliminates the compressive force component of Equation 43:

$$\frac{F}{A_i} = \sigma_r(\frac{A_o - A_i}{A_i} - 2) \qquad (54)$$

$$F = \sigma_r(A_o - 3A_i) \qquad (55)$$

$$F = 0 \rightarrow A_o = 3A_i \qquad (56)$$

$$\frac{D_o}{D_i} = \sqrt{3} \qquad (57)$$

Equation 57 shows that zero/negative mean stress is not a function of the radial stress but instead only of the ratio of outer to inner diameters of the specimen. The diameter ratio for the specimens tested was two, meaning that a test of negative mean stress is possible. The theoretical lowest mean stress that can be achieved is one associated with the uniaxial tensile strength:

$$p = \frac{-T}{3} \qquad (58)$$

33

3.6 Experimental Setup

Dog-bone triaxial extension tests were performed using the MTS 815 Rock Mechanics Test System load frame with the MTS 286 pressure confining unit. In order to perform a triaxial extension test where the axial stress is less than the radial stress, the specimen needs to be isolated in the axial direction such that no confining pressure acts on the plane normal to the axis of the specimen. Stainless steel platens shown in Figure 21 were specifically designed for triaxial extension testing with the MTS load frame. The platens have grooves on the flange for O-rings and six bolt holes evenly positioned around the platen. Sealing, which means isolating the confining fluid to act only in the radial direction, is ensured by the O-rings at the platen-load cell and platen-actuator interfaces.
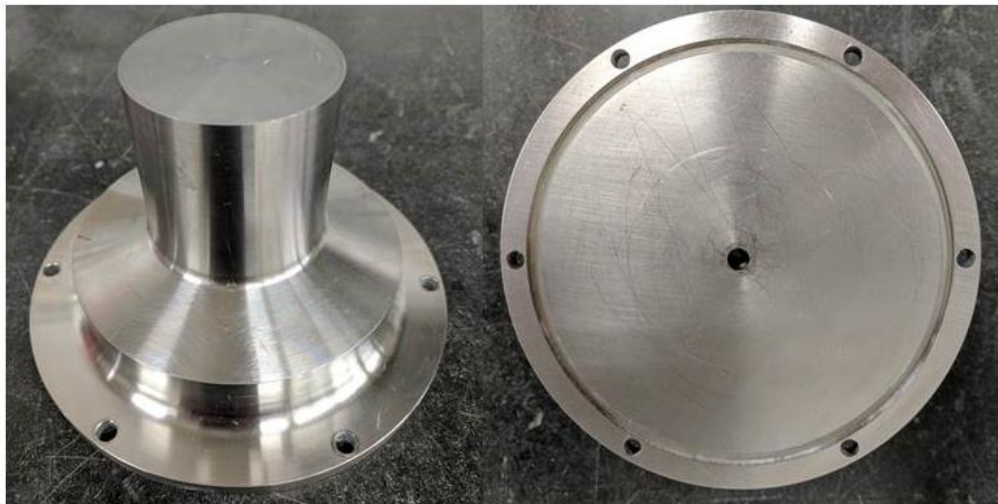
Figure 21. Stainless steel extension platens.

Typical triaxial tests use some form of pre-molded rubber membrane to seal the specimen from the confining fluid, but with the area change of a dog-bone specimen this is not easily accomplished. Instead, a thin layer of polyurethane was applied to the entire specimen and over the specimen-platen interfaces. The thin layer of polyurethane fully transfers the fluid pressure to the specimen and provides excellent sealing (Figure 22).

Figure 22. Polyurethane coated specimen with extension platens.

The load frame is equipped with an internal pressure equilibrated load cell that reads only deviator force and not the force that is applied from confining pressure. The load cell gives output in tension for the specimen to be in an extension stress state ($\sigma_r > \sigma_a$). When the internal load cell reads tension, it is not because the load cell is being pulled, but rather it is extending due to the force from the confining fluid being greater than the axial force from the specimen on the load cell. The deviator force that is read by the load cell is the sum of both force components in the axial direction of the dog-bone specimen plus a force taken by the polyurethane coating:
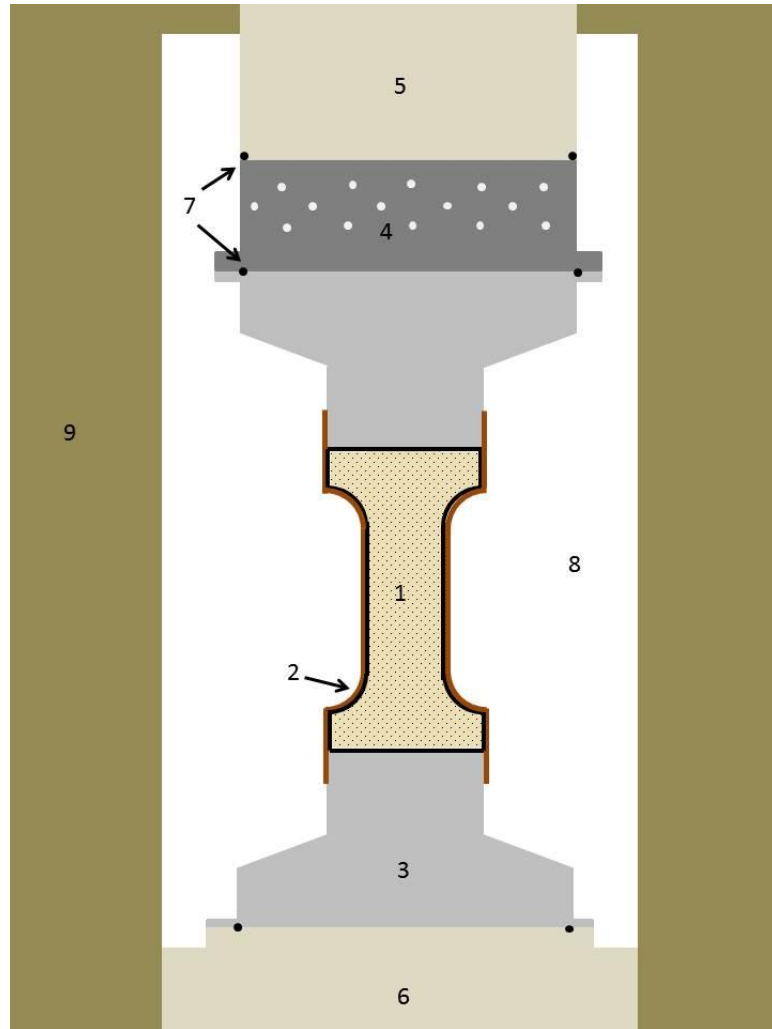
Figure 23. Dog-bone triaxial extension experimental schematic. (1) dog-bone specimen, (2) polyurethane coating, (3) stainless steel extension platens, (4) pressure equilibrated load cell, (5) loading rod, (6) actuator, (7) O-rings, (8) confining fluid, (9) pressure vessel.

$$F_D = F_1 + F_2 - F_{poly} \tag{59}$$

A pressure dependent force correction was applied to account for the thickness of the polyurethane coating t_{poly} on the specimen since the polyurethane does carry load:

$$F_{poly} = \frac{\pi}{4} \sigma_r [(D_i + 2t_{poly})^2 - D_i^2] \tag{60}$$

The force taken by the polyurethane coating is added to the deviatoric force output:

$$\sigma_a = \frac{F_D + F_{poly}}{A_i} + \sigma_r \tag{61}$$

Extension unloading was the stress path taken for all dog-bone tests, where the specimen is hydrostatically loaded to the desired radial stress, then the axial stress is unloaded to failure. The unloading was performed by displacement control at a rate of 0.5 micron per second. Axial strain was measured by resistive strain gages in the throat region at three locations separated by 120°. A thin layer of epoxy adhesive was applied to the surface of the specimen prior to strain gage application. The polyurethane coating covers the strain gages and lead wires (Figure 24).

Figure 24. Axial resistive strain gages on dog-bone specimen.

Chapter 4: Results and Discussion

4.1 Measurements of Elastic Parameters

The bulk modulus of Dunnville sandstone was measured on dog-bone specimens during the hydrostatic loading phase of the triaxial extension unloading stress path. The axial portion of mean stress was applied mechanically unlike the hydrostatic compression tests on right cylindrical specimens where both axial and radial stress was applied with confining fluid. Axial strain was reported using the average of three axial strain gages and radial strain was reported from a single gage.
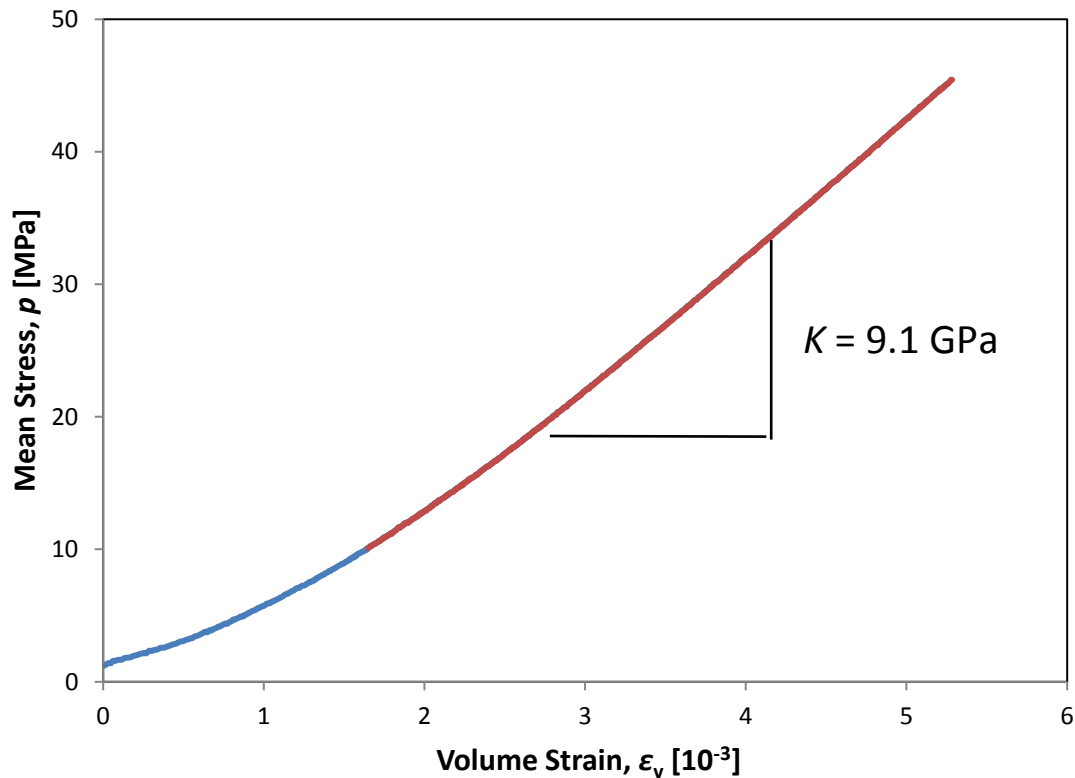

Figure 25. Measured bulk modulus during the hydrostatic loading of a dog-bone extension test.

Bulk modulus was measured on three dog-bone specimens and yielded values of 9.9, 8.6, 9.1 GPa (Figure 25). These values match well with the results from right cylindrical specimens reported in Table 1. This result also gives confidence in the axial stress correction from Equation 61.

Deformation was measured during the deviatoric (unloading) phase of the dog-bone triaxial extension stress path. Figure 26 shows an axial stress − axial strain curve from a hydrostatic state of stress (p = 20 MPa) to a post-failure stress state. The specimen behaved elastically from σ_a = 20 − 12 MPa. Yield occurred at σ_a < 12 MPa.

Figure 27a shows the Young's modulus in extension under a constant radial stress of 20 MPa. Young's modulus was measured on dog-bone specimens at various radial stresses and compared to values measured under triaxial compression in Figure 27b, where the two smallest values of mean stress correspond to Young's modulus under uniaxial compression and tension. The axial stress component of the mean stress reported is the average stress from the linear portion of the load/unload curve.

Figure 27b shows that both in extension and compression Young's modulus plateaus once the mean stress is large enough. The variation in E near constant value is due to microcracks closing under pressure, where under low mean stress pre-existing cracks are not closed and therefore the rock is not as stiff.

(a)
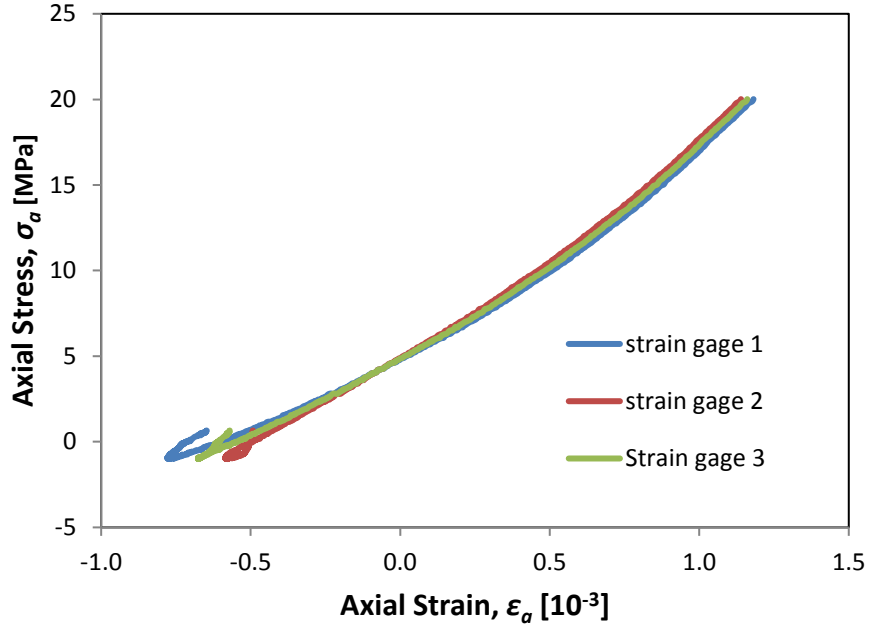
(b)
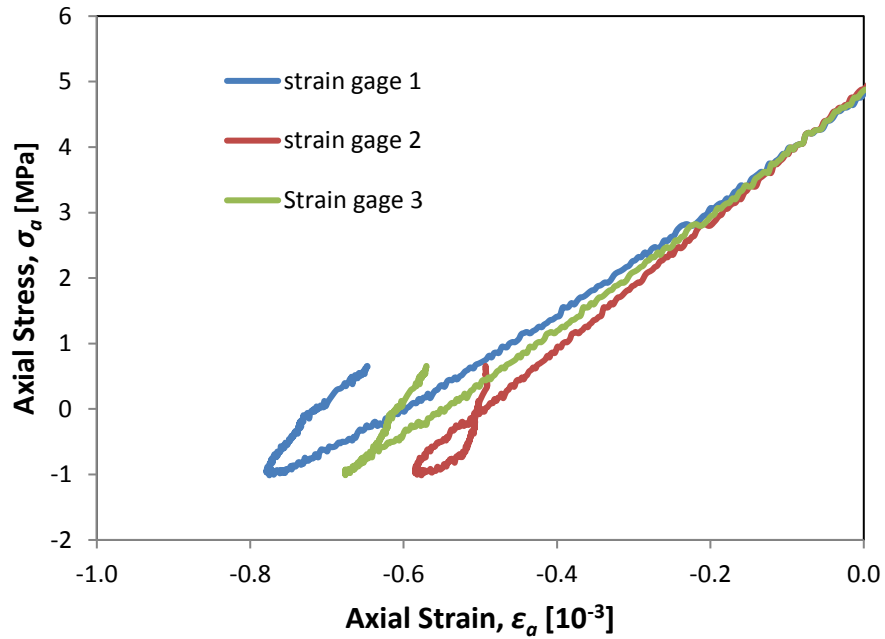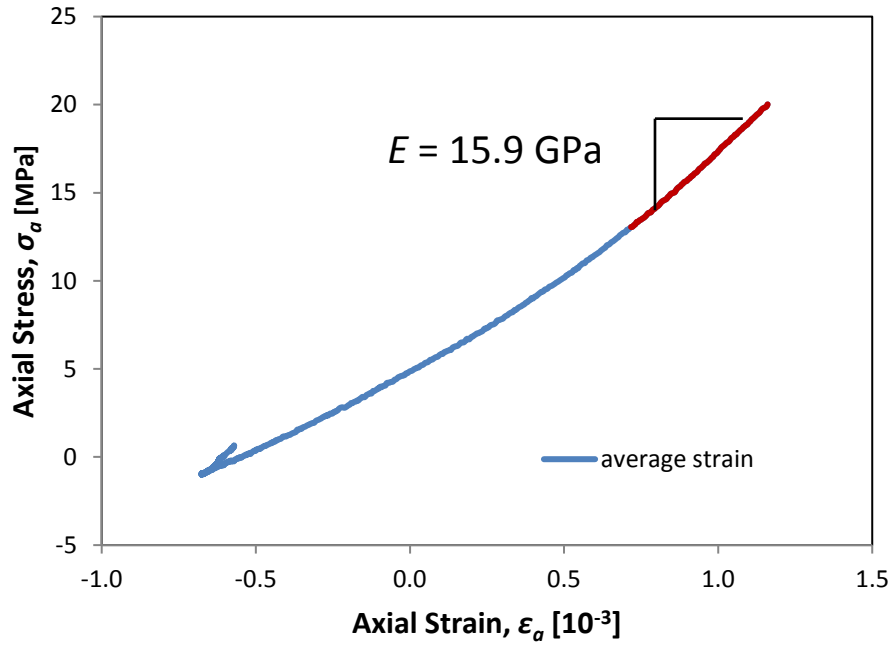

Figure 26. Axial stress – axial strain curves for a dog-bone specimen, DB4, under 20 MPa confining pressure. (a) Complete stress-strain behavior. (b) Response at failure.
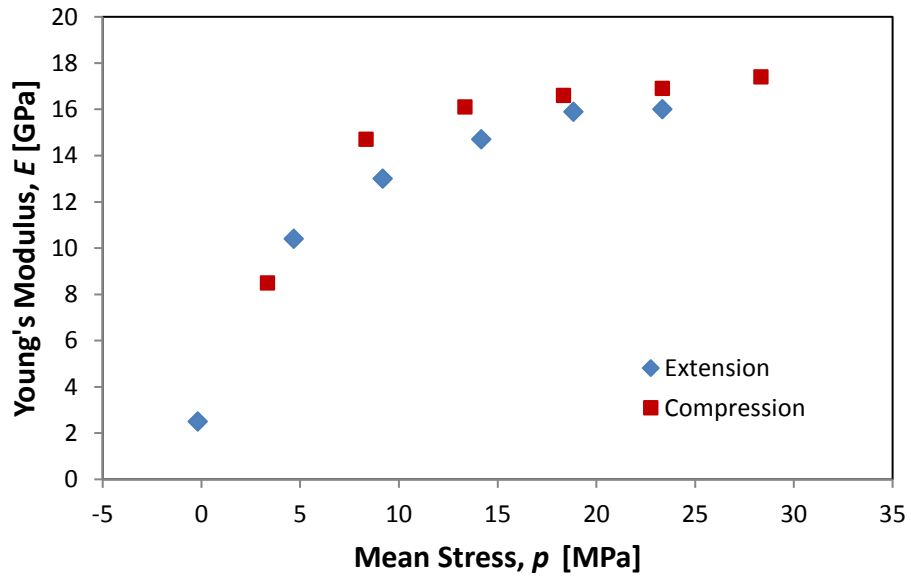
(a)

(b)

Figure 27. (a) Average axial stress – axial strain response for a dog-bone specimen under 20 MPa confining pressure. (b) Comparison of Young's Modulus versus mean stress in extension and compression.
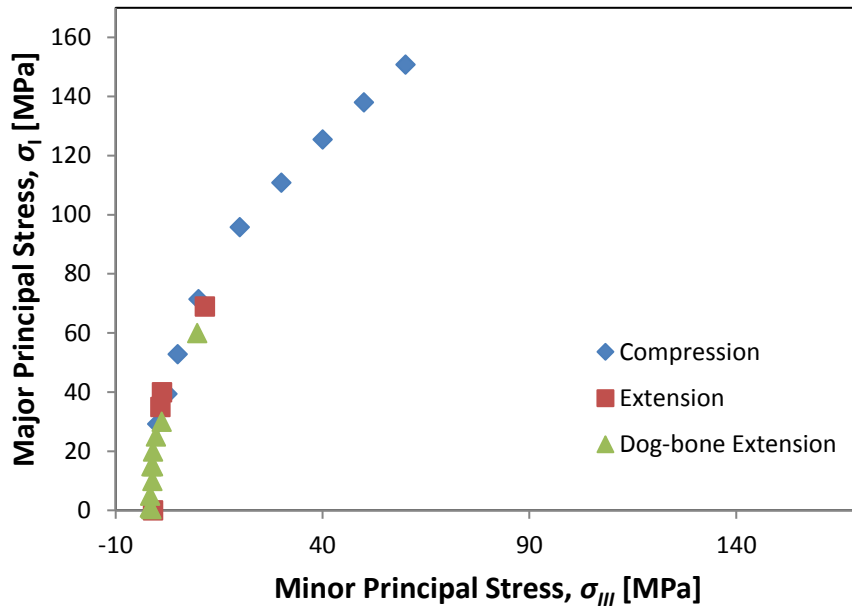
4.2 Failure Criteria Fitting

Eleven dog-bone specimens were tested under the triaxial extension unloading stress path with nine of the specimens having one principal stress in tension and seven in the low mean stress regime (Table 2). Figures 28 and 29 show the dog-bone triaxial extension data in comparison with nine conventional triaxial compression and four conventional triaxial extension tests.

Table 2. Failure stresses of eleven dog-bone triaxial extension specimens

Specimen	σ_a [MPa]	σ_r [MPa]	p [MPa]	q [MPa]
DB 9	-1.40	0.5	-0.13	-1.90
DB 12	-1.50	0.75	0.00	-2.25
DB 5	-1.79	1.0	0.07	-2.79
DB 8	-1.66	5.0	2.78	-6.66
DB 2	-1.11	10.0	6.30	-11.11
DB 7	-1.38	15.0	9.54	-16.38
DB 3	-1.02	15.0	9.66	-16.02
DB 4	-1.01	20.0	13.00	-21.01
DB 6	-0.26	25.0	16.58	-25.26
DB 17	1.11	30.0	20.37	-28.89
DB 14	9.69	60.0	43.23	-50.31

It can be seen in Figure 28b that the uniaxial tensile strength is smaller in magnitude than some of the minor principal stresses of the dog-bone extension tests. This can be attributed to variation in the rock, as well as the difference in testing procedure and apparatus between the two different types of tests. Also, it is difficult to eliminate bending in uniaxial tension.

(a)
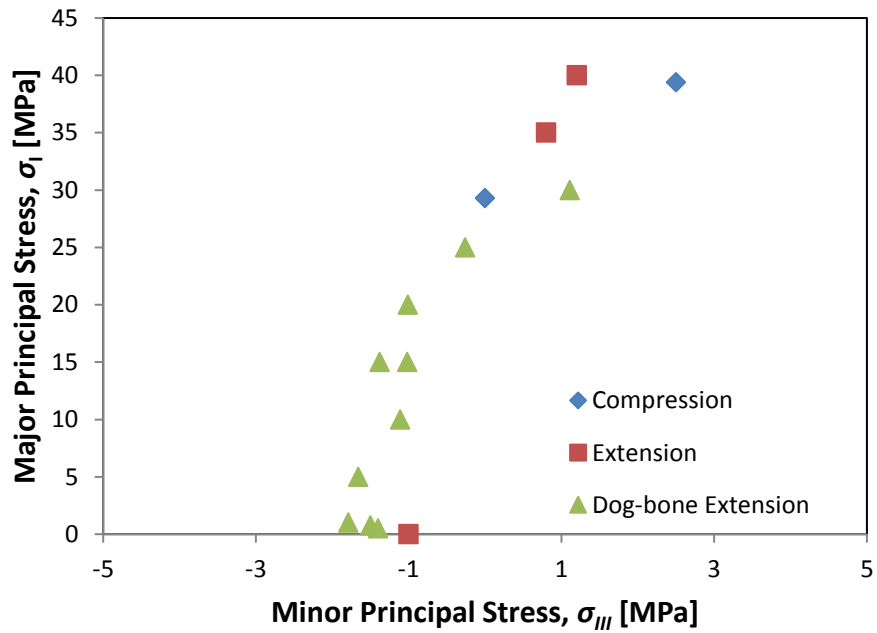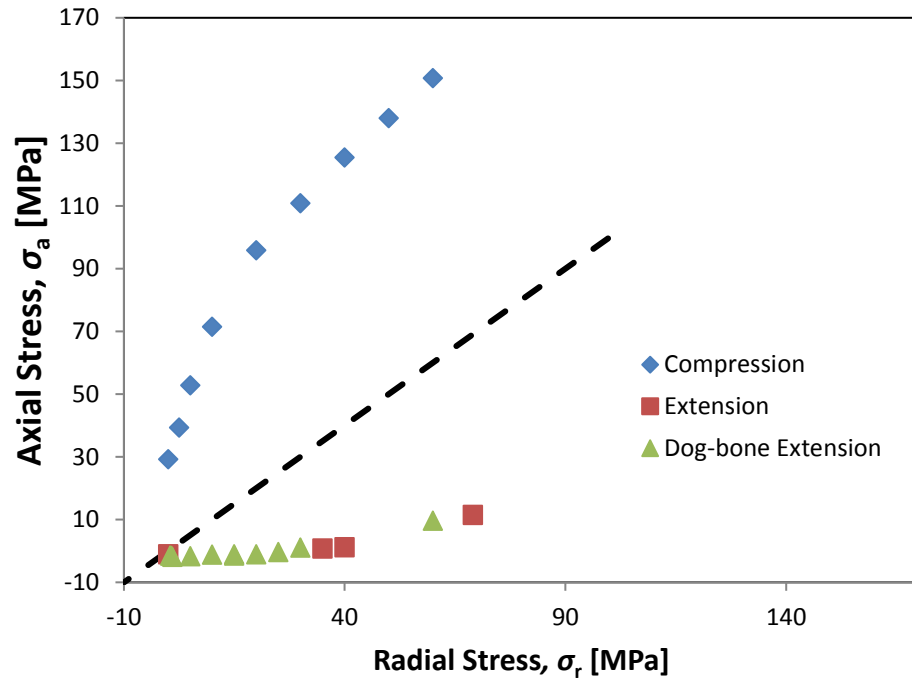

(b)

Figure 28. (a) Experimental failure data in σ_I-σ_{III} plane. (b) Close-up of low mean stress region.
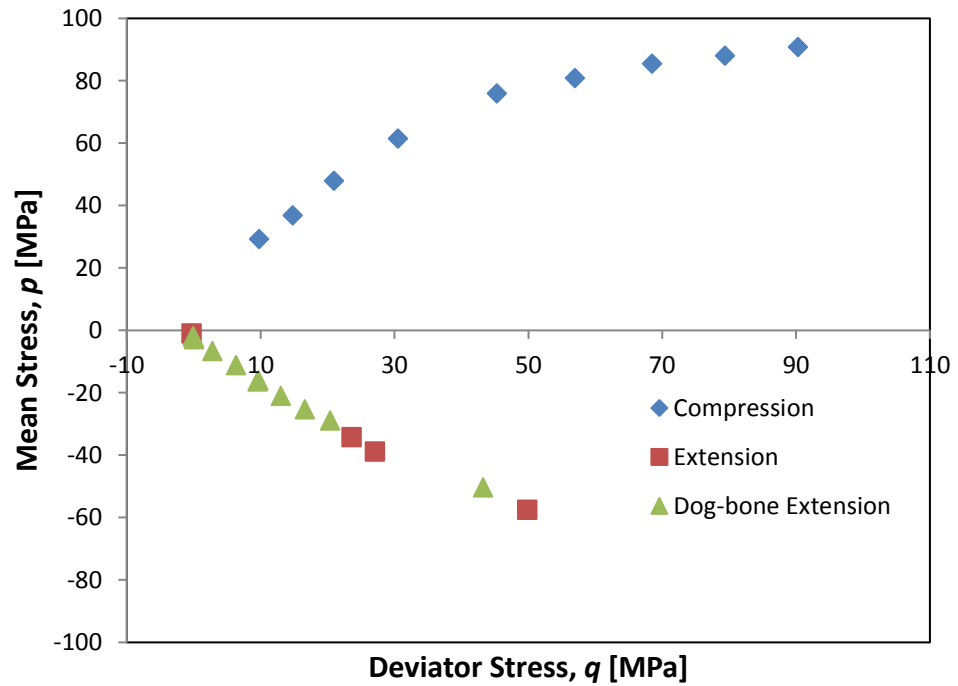
(a)

(b)

Figure 29. Experimental failure data in (a) σ_a-σ_r plane, (b) p-q plane.

The four different failure criteria were fitted using appropriate methods for each criterion: linear least squares (*MC*), plane fitting (*PMC*), non-linear least squares (*HB* and *Fh*). For Mohr-Coulomb and Paul-Mohr-Coulomb, the measured direct tensile strength was used as a third and fourth parameter respectively instead of assuming a uniaxial strength ratio *n*. The Fairhurst tensile strength was determined as one of the fitted parameters for the criterion. The fitted values are listed in Table 3.

Table 3. Fitted parameters for Mohr-Coulomb, Paul-Mohr-Coulomb, Hoek-Brown, and Fairhurst failure criteria.

Failure Criteria	Parameter 1	Parameter 2	Parameter 3	Parameter 4
Mohr-Coulomb	$C_0 = 32.9$ MPa	$\phi = 22.4$ °	$T = 1.0$ MPa	N/A
Paul-Mohr-Coulomb	$V_0 = 23.6$ MPa	$\phi_c = 23.4$ °	$\phi_e = 24.0$ °	$T = 1.0$ MPa
Hoek-Brown	$C_0 = 29.3$ MPa	$m_b = 5.9$	N/A	N/A
Fairhurst	$C_0 = 32.9$ MPa	$T_0 = 1.5$ MPa	N/A	N/A

The four different criteria fits are shown in Figures 31-34 in the σ_a-σ_r plane. It can be seen that both linear failure criteria struggle to capture the failure envelope over the range of radial stresses that were used in this study. The linear criteria are conservative at small radial stresses and then become incautious at larger confining stresses. The nonlinear criteria also appear to have this trait, but not to the degree of the linear criteria.
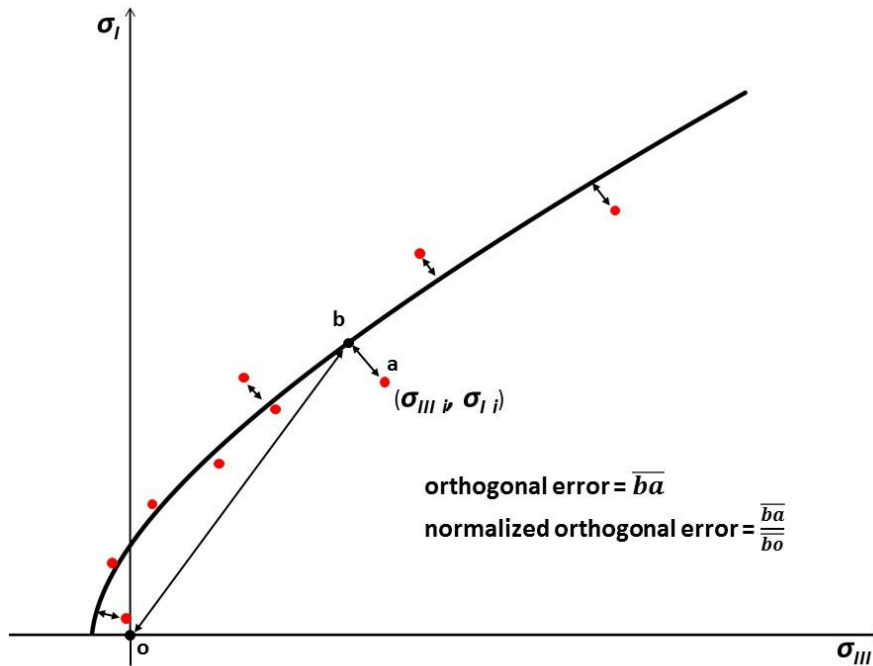
Figure 30. Normalized orthogonal error determination.

It is also evident that the three criteria that use the tension cut-off more accurately capture the low mean stress regime compared with the Hoek-Brown criterion. Table 4 provides a breakdown of the error in different (preassigned) stress regimes. The orthogonal distance from the prediction to the data point, the error, was normalized by the distance from the origin to the point on the failure surface that corresponds to the data (Figure 30). The linear failure criteria have higher error in the high mean stress ($p \geq C_0$) regime, but the error is small at low mean stress ($p < C_0/3$) because of the tension cut-off. Hoek-Brown does a better job predicting failure at high mean stress than low mean stress. The Fairhurst criterion shows the smallest error. This is because the tension cut-off has shown to work best for low mean stress and a nonlinear criterion is best in the high mean stress regime.

46

Table 4. Normalized orthogonal error per data point for the four different failure criteria under different stress regimes: low mean stress $p < C_0/3$, high mean stress $p \geq C_0/3$, tensile-compressive $\sigma_a < 0 \leq \sigma_r$, compressive-compressive $0 < \sigma_a$, $0 \leq \sigma_r$.

Failure Criteria	Low mean stress [MPa]	High mean stress [MPa]	$\sigma_a < 0 \leq \sigma_r$ [MPa]	$0 < \sigma_a$, $0 \leq \sigma_r$ [MPa]	Total [MPa]
Mohr-Coulomb	0.07	0.08	0.06	0.09	0.08
Paul-Mohr-Coulomb	0.06	0.04	0.05	0.04	0.05
Hoek-Brown	0.46	0.03	0.37	0.03	0.17
Fairhurst	0.01	0.02	0.02	0.02	0.02

Figure 31. Fitted Mohr-Coulomb failure criterion in σ_a-σ_r plane.

Figure 32. Fitted Paul-Mohr-Coulomb failure criterion in σ_a-σ_r plane.

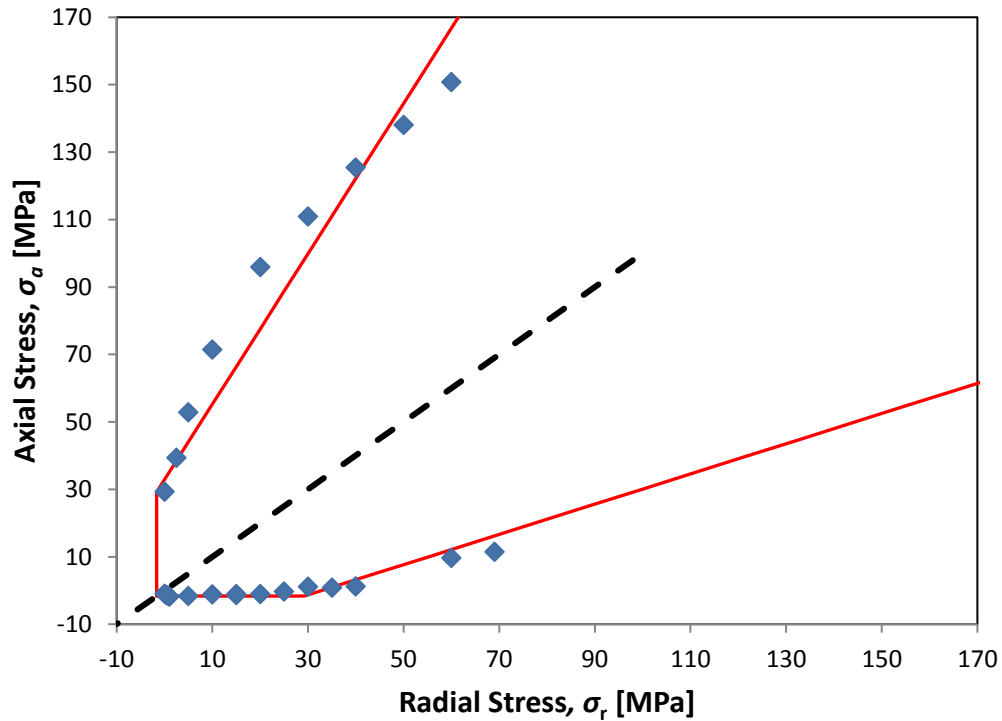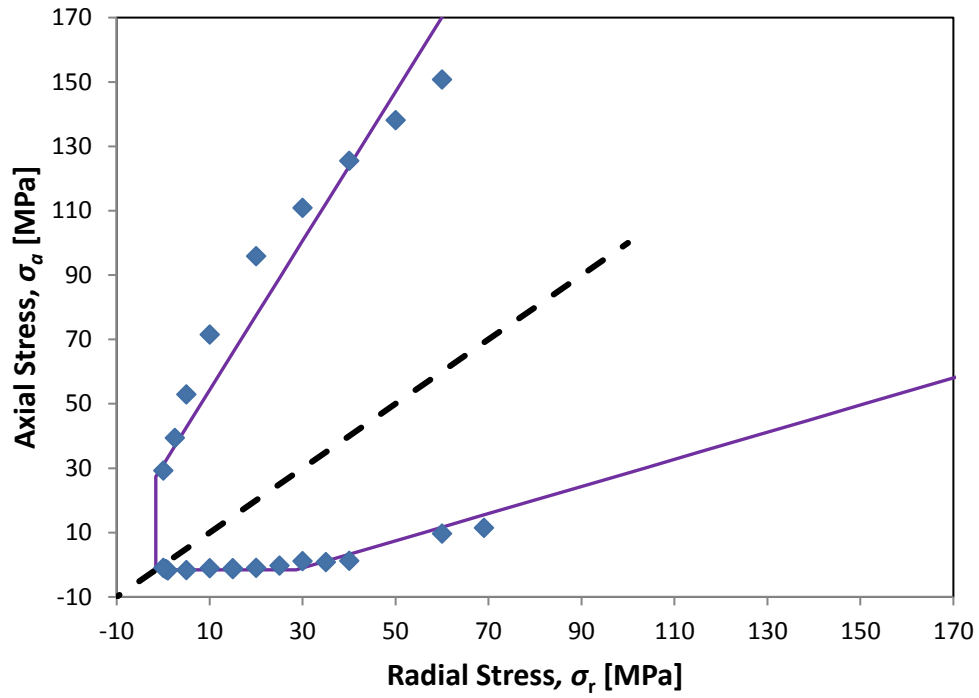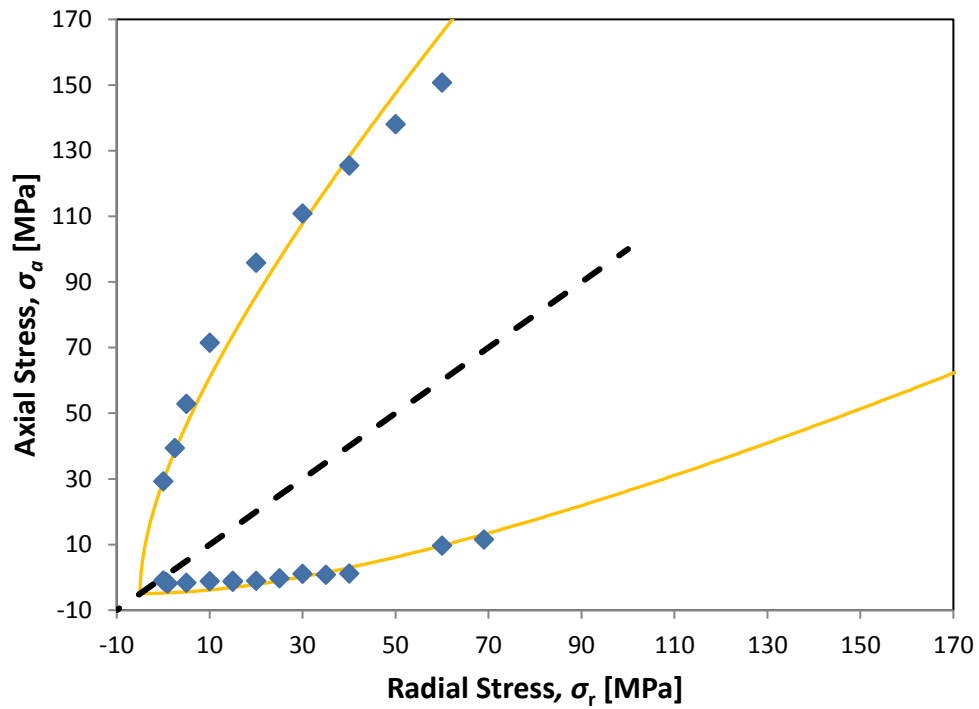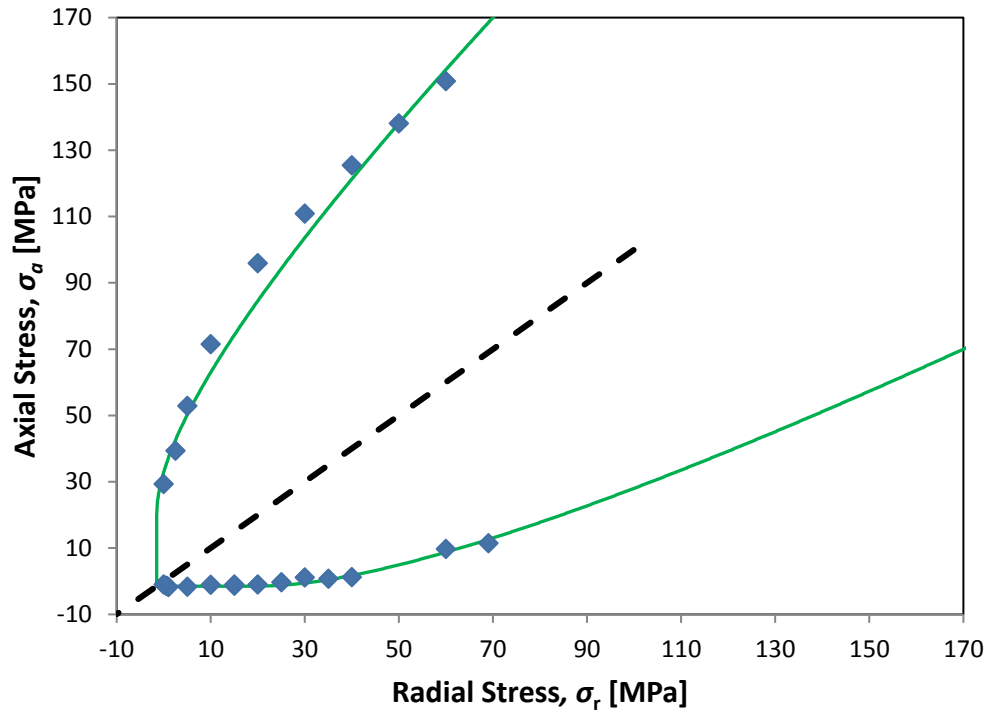Figure 33. Fitted Hoek-Brown failure criterion in σ_a-σ_r plane.

Figure 34. Fitted Fairhurst failure criterion in σ_a-σ_r plane.
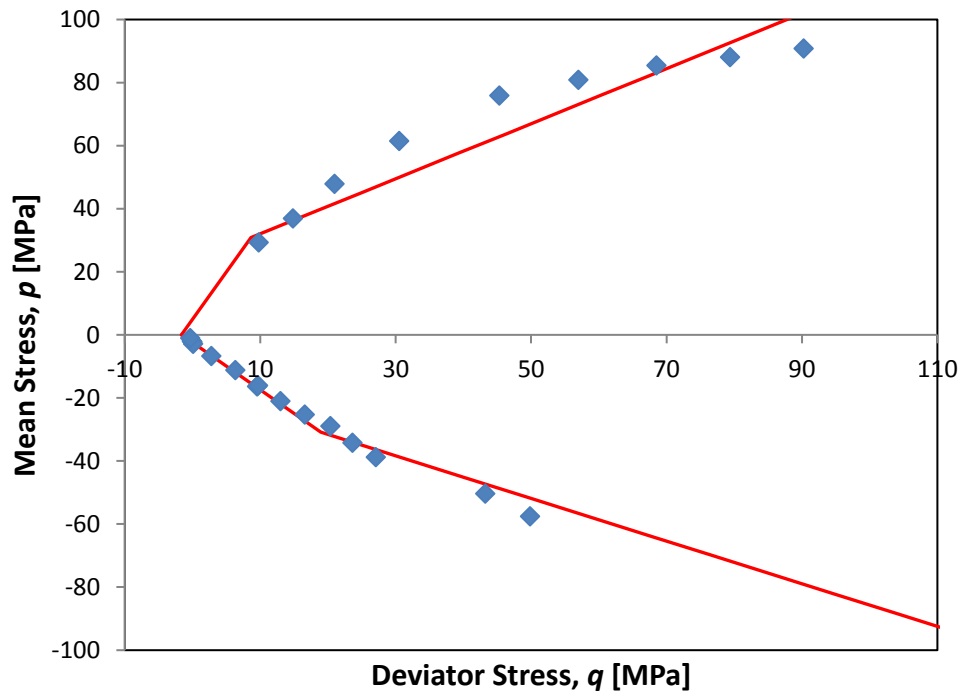
Figure 35. Fitted Mohr-Coulomb failure criterion in p-q plane.
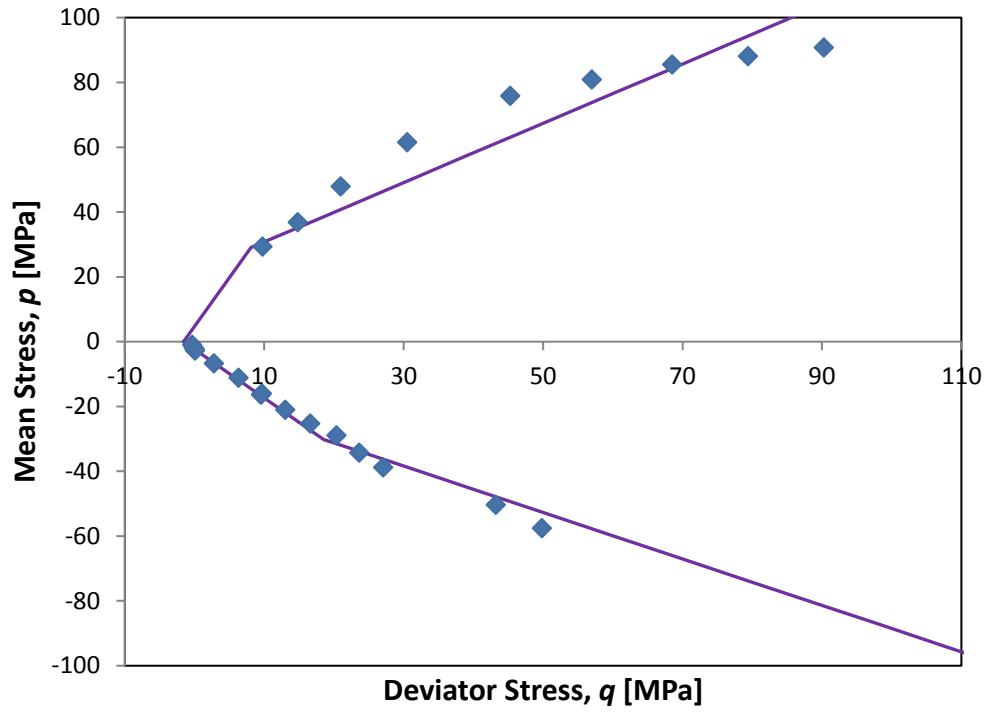
Figure 36. Fitted Paul-Mohr-Coulomb failure criterion in *p-q* plane.
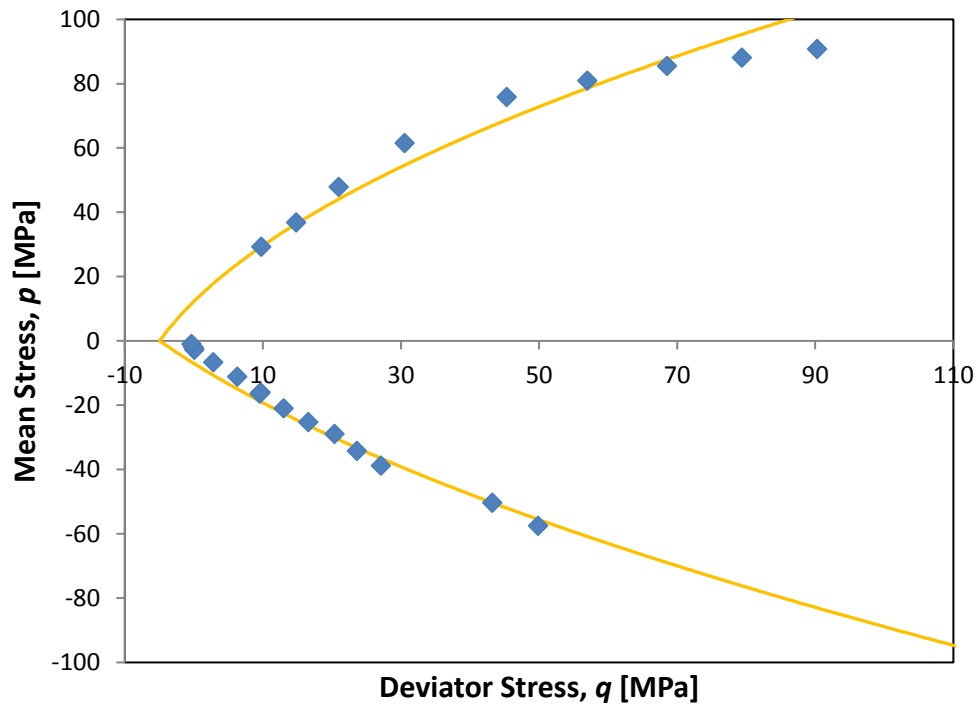
Figure 37. Fitted Hoek-Brown failure criterion in *p-q* plane.

50
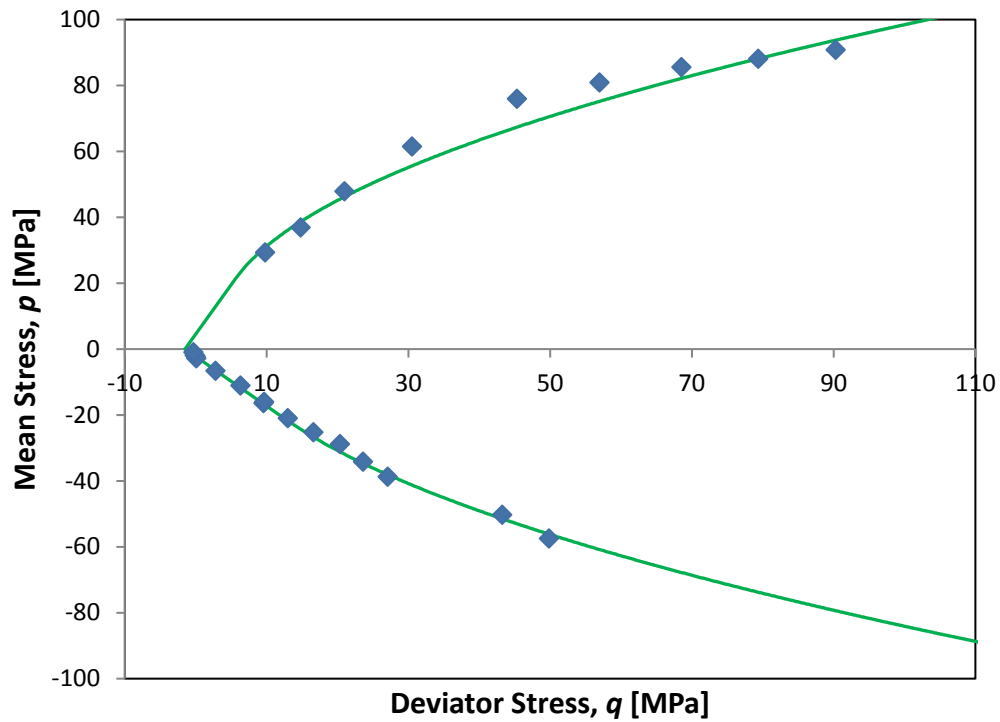
Figure 38. Fitted Fairhurst failure criterion in *p-q* plane.

4.3 Fracture Properties

Three dog-bone specimens were tested at high mean stress with all three principal stresses compressive in order to ensure that shear fracture developed in extension. All three of these dog-bone tests, the three largest mean stresses in Figure 39a, exhibited shear fracture, and as others (Ramsey and Chester, 2004) have shown, the fracture angle in extension increases with mean stress. The fracture angle is measured between the normal to the fracture surface and the minimum principal stress direction (Fig. 39b). In the low mean stress regime, there appears to be little to no correlation between fracture angle and mean stress, because all of the low mean stress specimens have angles varying between 2° and 10°.

(a)
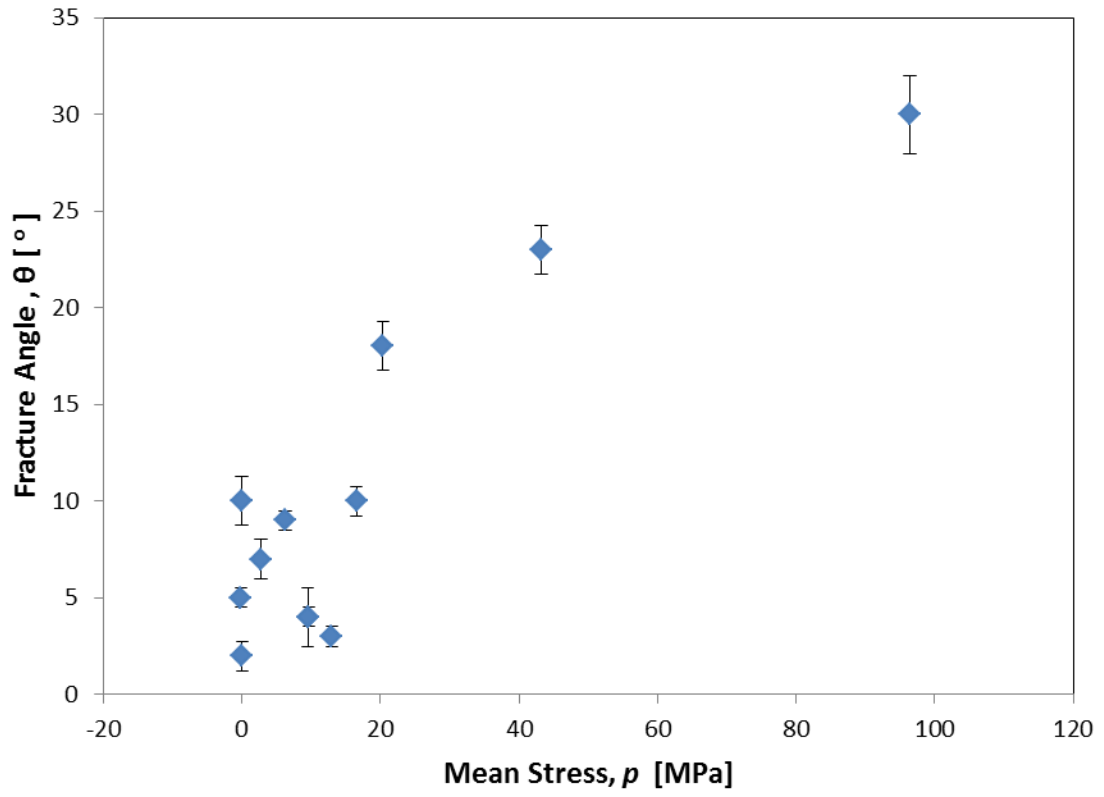
(b)
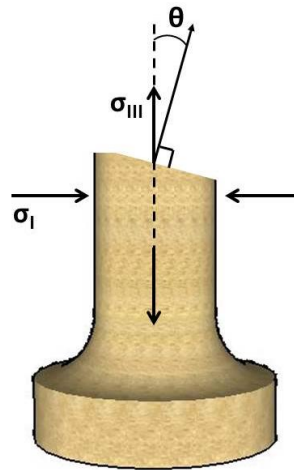
Figure 39. (a) Fracture angle versus mean stress on dog-bone specimens. Error bars are one standard deviation. (b) Fracture angle orientation.

Since the orientation of the low mean stress fractures had little correlation, the individual fracture surfaces were analyzed for surface roughness to gain insight on the failure mode. Figure 40 shows six dog-bone fracture surfaces with increasing mean stress. The two specimens failed under high mean stress show crushed grains, suggesting a shear fracture formed. The two specimens failed under low mean stress show little to no signs of sliding as the fracture surfaces appear to be clean; this would suggest tensile (opening mode) failure.
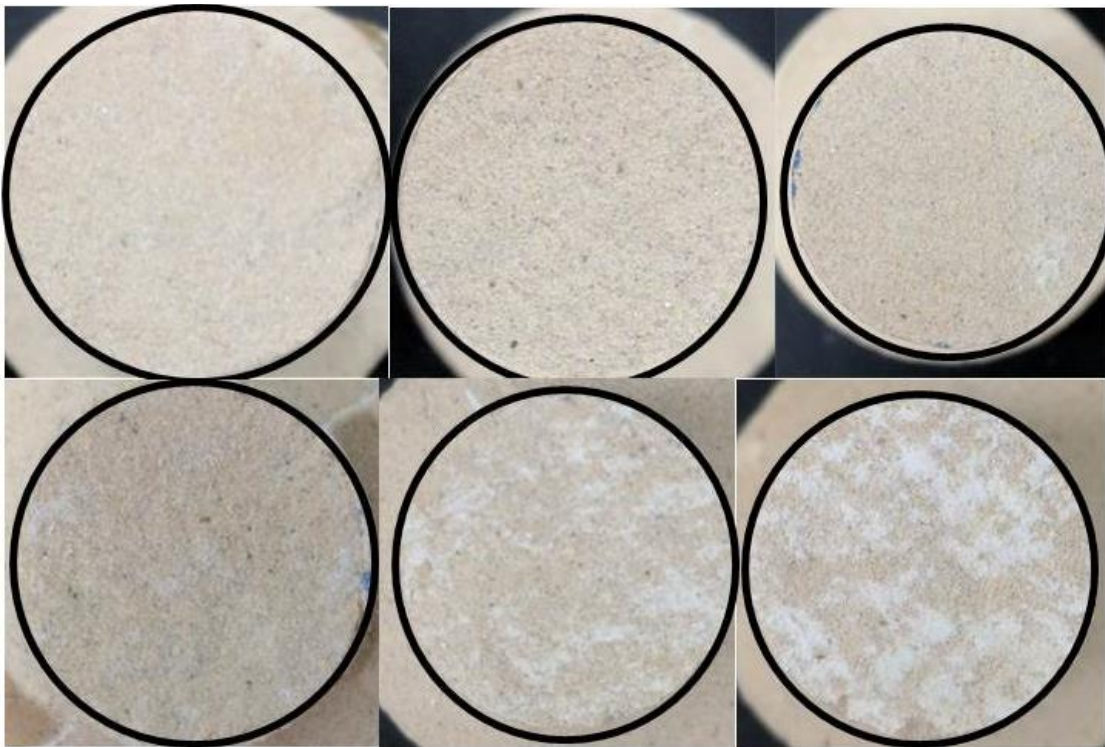
Figure 40. Photographs of dog-bone fracture surfaces immediately after testing with increasing mean stress from top left to lower right ($p = 0.0, 0.1, 6.3, 13.0, 20.4, 43.2$ MPa).

The fracture surfaces of eight dog-bone specimens, one uniaxial tension specimen, and one triaxial compression specimen were analyzed using a HP 3D Scanner Pro S3. The

scanner uses enhanced structured light scanning technology and an automatic 360° turntable to create a 3D model. The scanner resolution is 50 microns between vertices and each scan can have up to 2.3 million vertices. The scan can be edited using David 3D Scanner Pro software to only show vertices on the fracture surface.

The scans were used to estimate the surface roughness of the fracture surfaces (Figure 42), with the hypothesis that a tension fracture (opening mode) would have a larger surface roughness parameter than a shear fracture (sliding mode). The vertices were formulated into triangles and the surface area of an individual triangle was calculated using the cross product:

$$A_i = \frac{1}{2}\left\|\overline{ba} \times \overline{bc}\right\| \tag{62}$$

A surface roughness parameter R was determined using the sum of the individual triangle areas and a reference area of the surface:

$$R = 1 - \frac{1}{A_{ref}}\sum_i A_i \tag{63}$$

The scans were performed at a resolution of 50 micron between vertices. The reference area A_{ref} was also calculated using Equation 62, but from a scan resolution of 500 microns. This was done to allow for larger irregularities in the fracture surface to not affect the surface roughness parameter.
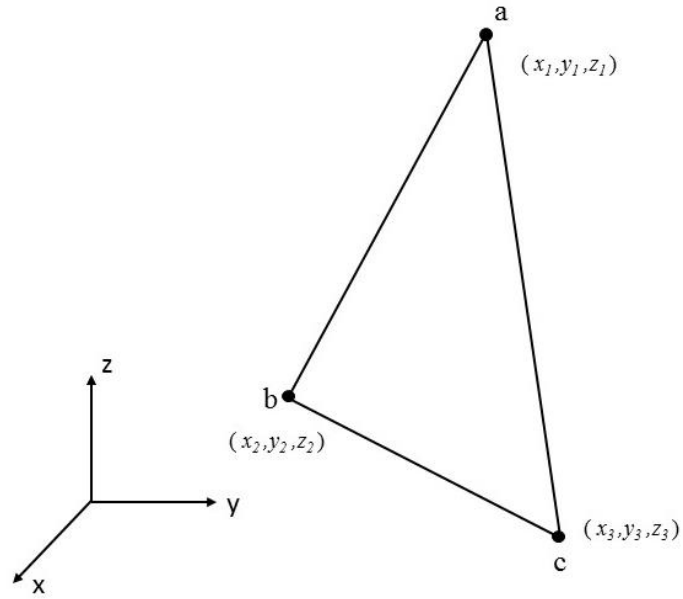
Figure 41. Area determination of a triangle in 3-dimensional coordinate system.
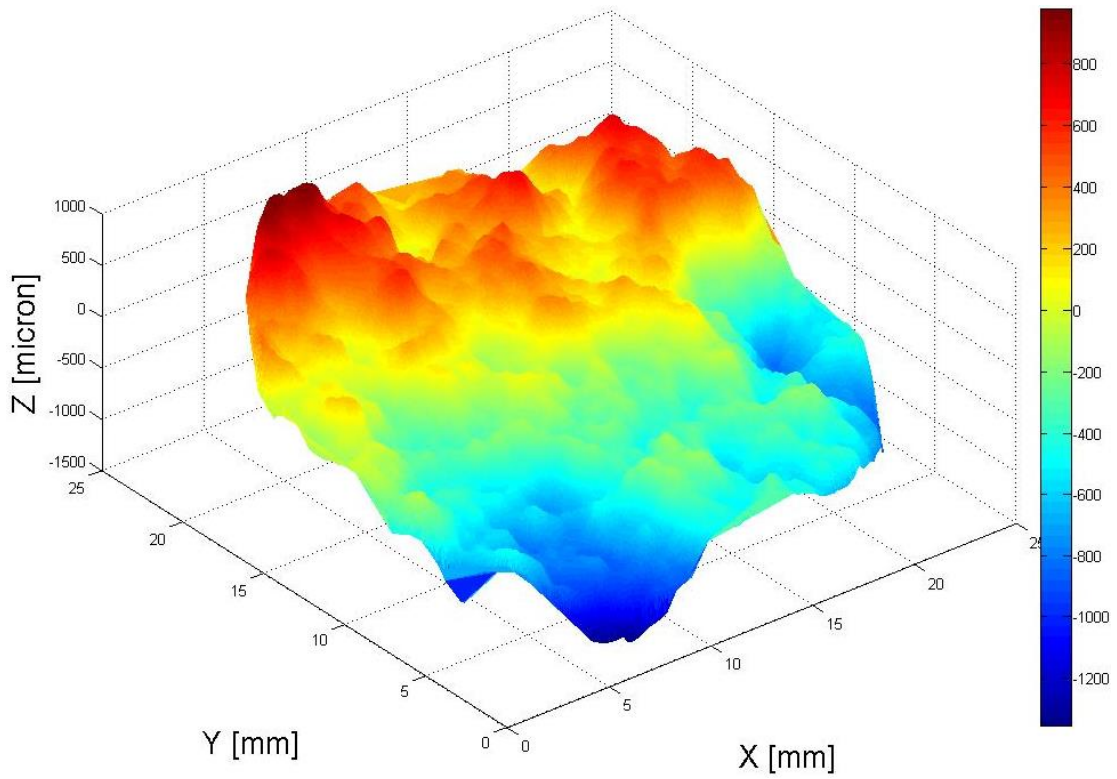
Figure 42. Contour of scanned fracture surface.

Figure 43 shows the correlation between the surface roughness and mean stress. A specimen that failed by tensile (opening mode) fracture has a rougher surface than one failed by shear. The dog-bone specimens that failed under low mean stress appear to follow a transition from the surface roughness of tensile failure to shear failure, as opposed to having similar surface roughness to either the tension failure or shear failure.
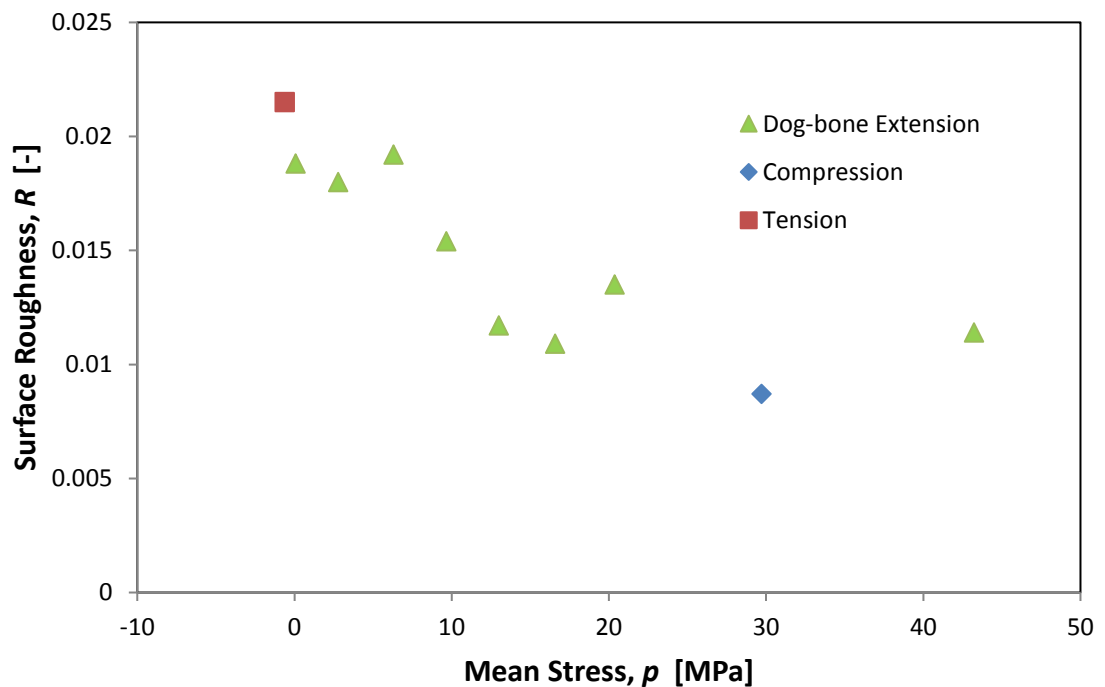
Figure 43. 3D scanned fracture surface roughness versus mean stress.

Chapter 5: Conclusions

Little data exist on failure of rock at low mean stress or under a stress state with one tensile principal stress. Triaxial tests were performed with a dog-bone specimen, which involves a geometry of different cross-sectional area, such that the differential area provides an opportunity to generate a tensile force in the axial direction. Stress states with mean stress $p = (\sigma_1 + \sigma_2 + \sigma_3)/3$ ranging from $p = -T/3 = -0.3$ MPa for uniaxial tension to $p = C_0/3 = 9.8$ MPa for uniaxial compression were achieved, where $T =$ uniaxial tensile strength and $C_0 =$ uniaxial compressive strength. Conventional triaxial compression and extension tests on dry Dunnville sandstone were used in conjunction with dog-bone extension tests.

Two linear and two nonlinear, with respect to principal stresses, failure criteria were fit to the data. The linear failure criteria, Mohr-Coulomb and Paul-Mohr-Coulomb both with tension cut-offs, fit the high mean stress ($p > C_0/3$) data poorly, but fit the low mean stress data well because of the implementation of the tension cut-off. The Hoek-Brown criterion did a poor job with the low mean stress data, as it over estimated the tensile strength, but did a good job fitting the high mean stress data. The Fairhurst criterion provided the best overall fit because it is nonlinear, which works well for high mean stress states, and has a natural tension cut-off, which was proven to work best for the low mean stress states.

The fracture surfaces were analyzed using a 3D scanner to gather insight on the failure mode at various levels of mean stress. Visual signs of shear-type failure were observed in specimens failed under high mean stress, and no such signs of shearing were observed in specimens at low mean stresses. A surface roughness parameter was defined based on a surface area ratio and showed that specimens failed at low mean stresses exhibited a higher surface roughness than those failed at high mean stresses, and there was a transition from opening mode fracture to shear fracture. This transition could be considered a hybrid fracture given the nature of the principal stresses at failure.

From the combination of failure and surface roughness analyses, the results showed that at low mean stresses tension was the main failure mode and a tension cut-off is the best form of predicting failure at low mean stresses.

The work done in this study can be expanded for different types of rocks. These studies should look into the surface roughness parameter's dependence on stress state. Also, more failure criteria should be used for analysis to determine if one can better characterize the failure envelope in the low mean stress regime.

References

Brace, W.F. 1964. Brittle fracture of rocks. In: Judd WR (ed) *State of stress in Earth's crust*. Elsevier, New York, 111-188.

Bridgman, P.W. 1937. Breaking Tests under Hydrostatic Pressure and Conditions of Rupture. *Phil. Mag*. Vol. 24, pp. 63-80.

Carter, B.J., E.S. Duncan, and E.Z. Lajtai. 1991. Fitting strength criteria to intact rock. *Geotechnical & Geological Engineering* 9.1: 73-81.

Cornet F. H. and Fairhurst C. 1974. Influence of pore pressure on the deformation behaviour of saturated rocks. *Proc. of the 3rd Congress of the Int. Soc. for Rock Mech.*, Vol. I(B), pp. 638-644

Corthésy, R., and M. H. Leite. 2008. A strain-softening numerical model of core discing and damage. *International Journal of Rock Mechanics and Mining Sciences* 45.3: 329-350.

Coulomb, C. A. 1776. *Essai sur une application des règles de maximis & minimis à quelques problèmes de statique, relatifs à l'architecture*. De l'Imprimerie Royale.

Fairhurst, C. 1964. On the validity of the 'Brazilian' test for brittle materials. *International Journal of Rock Mechanics and Mining Sciences & Geomechanics* Abstracts. Vol. 1. No. 4. Pergamon.

Griffith, A. A. 1924. The theory of rupture. *Appl. Mech. Proc. Int. Congr*., 1st, 55-63.

Goodman, Richard E. 1989. *Introduction to rock mechanics*. Vol. 2. New York: Wiley.

Hoek, E. and E.T. Brown. 1980. Empirical strength criterion for rock masses. *Journal of Geotechnical and Geoenvironmental Engineering* 106.ASCE 15715.

Hoek, Evert.1983. Strength of jointed rock masses. *Geotechnique* 33.3: 187-223.

Hoek, Evert. The Hoek-Brown failure criterion-a 1988 update. 1988. *Proc. 15th Canadian Rock Mech. Symp*. Toronto, Dept. Civil Engineering, University of Toronto.

Hoek, E. Estimating Mohr-Coulomb friction and cohesion values from the Hoek-Brown failure criterion. 1990 *International Journal of Rock Mechanics and Mining Sciences & Geomechanics Abstracts*. Vol. 27. No. 3. Pergamon.

Hoek, E. 1994. Strength of rock and rock masses. *ISRM News Journal* 2.2: 4-16.

Hoek, E., C. Carranza-Torres, and B. Corkum. 2002. Hoek-Brown failure criterion-2002 edition. *Proceedings of NARMS*-Tac 1: 267-273.

Hoek, E., and C. D. Martin. 2014. Fracture initiation and propagation in intact rock–a review. *Journal of Rock Mechanics and Geotechnical Engineering* 6.4: 287-300.

Hoek, E., and C. D. Martin. 2014. Fracture initiation and propagation in intact rock–a review. *Journal of Rock Mechanics and Geotechnical Engineering* 6.4: 287-300.

Jaeger, J. C., and E. R. Hoskins. 1966. Rock failure under the confined Brazilian test. *Journal of Geophysical research* 71.10: 2651-2659.

Jaeger, J. C., and N. G. W., Cook. 1979. Fundamentals of Rock Mechanics. Chapman and Hall, London.

Karman, T.H. Von. 1911. Festigkeitsversuche unter allseitigem Druck, Z. *Ver. Dt. Ing.*, 55, 1749-57.

Labuz, J.F. and J.M. Bridell. 1993. Reducing frictional constraint in compression testing through lubrication. *International journal of rock mechanics and mining sciences & geomechanics* abstracts. Vol. 30. No. 4. Pergamon.

Meyer, J.P. and J.F. Labuz. 2013. Linear failure criteria with three principal stresses. *International Journal of Rock Mechanics and Mining Sciences* 60: 180-187.

Mohr, O. 1900. Welche Umstände bedingen die Elastizitätsgrenze und den Bruch eines Materials. *Zeitschrift des Vereins Deutscher Ingenieure*,*46*(1524-1530), 1572-1577

Murrell, S.A.F. 1965. The effect of triaxial stress systems on the strength of rocks at atmospheric temperatures. *Geophysical Journal International*. 10.3: 231-281.

Nadai A. 1950. Theory of Flow and Fracture of Solids. NewYork:McGraw-Hill.

Nayak, Gyan C., and Olgierd C. Zienkiewicz. 1972. Convenient form of stress invariants for plasticity.

Pariseau, W.G. 2007. Fitting failure criteria to laboratory strength tests. *International Journal of Rock Mechanics and Mining Sciences* 44.4: 637-646.

Paul, B. 1960. Modification of the Coulomb-Mohr theory of fracture. *J Appl Mech*. 28:259-268.

Paul, B. 1968. Generalized pyramidal fracture and yield criteria. *International Journal of Solids and Structures* 4.2: 175-196.

Pincus, H.J. 2000. Closed-form/least-squares failure envelopes for rock strength. *International Journal of Rock Mechanics and Mining Sciences* 37.5: 763-785.

Ramsey, J.M. and F.M. Chester. 2004. Hybrid fracture and the transition from extension fracture to shear fracture. *Nature* 428.6978: 63-66.

Schock, R. N., and H. Louis. 1982. Strain behavior of a granite and a graywacke sandstone in tension. *Journal of Geophysical Research: Solid Earth* 87.B9: 7817-7823.

Tarokh, A., Y. Li, and J.F. Labuz. 2016. Hardening in porous chalk from precompaction. *Acta Geotechnica*: 1-5.

Voigt, Woldemar. 1899. Beobachtungen über Festigkeit bei homogener Deformation, angestellt von L. Januszkiewicz. *Annalen der Physik* 303.2: 452-458.

You, Mingqing. 2015. Strength criterion for rocks under compressive-tensile stresses and its application. *Journal of Rock Mechanics and Geotechnical Engineering* 7.4: 434-439.

You, Mingqing. 2010. Strength and failure of rock due to hydraulic fracture. *Rock stress and earthquakes*. Taylor & Francis, London: 185-188.

Appendix A – Tables of Rock Properties

Table 5. Density measurements.

Test	Density, ρ [g/cm^3]
1	1.809
2	1.815
3	1.803
4	1.810
5	1.813
6	1.804
7	1.790
8	1.807
9	1.792
10	1.793
11	1.807
12	1.780
13	1.786
14	1.789
Average	**1.800**
Standard Deviation	**0.011**

Table 6. Wave velocity measurements.

| Trial | Perpendicular | | Parallel | |
	P-Wave, V_p [m/s]	S-Wave, V_s [m/s]	P-Wave, V_p [m/s]	S-Wave, V_s [m/s]
1	1910	1059	1890	1064
2	1910	989	1990	1063
3	1920	1064	2010	1098
4	1930	1061	2033	N/A
5	1950	1053	2073	N/A
6	1960	N/A	2076	N/A
Average	**1930**	**1045**	**2012**	**1075**
Standard Deviation	**21**	**28**	**63**	**16**

Table 7. Uniaxial compressive strength measurements.

Test	UCS [MPa]
1	28.8
2	29.7
Average	**29.3**
Standard Deviation	**0.6**

Table 8. Poisson's ratio measurements.

Test	Poisson's Ratio, v [-]
1	0.33
2	0.32
3	0.31
4	0.28
5	0.29
6	0.30
7	0.30
8	0.30
9	0.34
10	0.34
11	0.34
Average	**0.31**
Standard Deviation	**0.02**

Table 9. Young's modulus in compression measurements.

Test	Young's Modulus, E [GPa]
1	8.2
2	8.1
3	8.1
4	8.5
Average	**8.2**
Standard Deviation	**0.2**

Table 10. Bulk modulus measurements.

Test	Bulk Modulus, K [GPa]
1	8.9
2	8.6
3	8.7
4	9.1
5	9.0
6	8.8
7	9.5
Average	**8.9**
Standard Deviation	**0.3**

Table 11. Uniaxial tensile strength measurements.

Test	Tensile Strength, T [MPa]
1	1.2
2	0.9
3	1.0
4	0.9
5	1.0
Average	**1.0**
Standard Deviation	**0.1**

Table 12. Brazilian tensile strength measurements.

Test	Brazilian Tensile Strength [MPa]
1	2.3
2	2.2
3	2.0
4	2.1
5	1.9
6	2.1
7	2.0
8	1.8
9	2.0
10	2.1
Average	**2.0**
Standard Deviation	**0.1**

Table 13. Young's modulus in tension measurements.

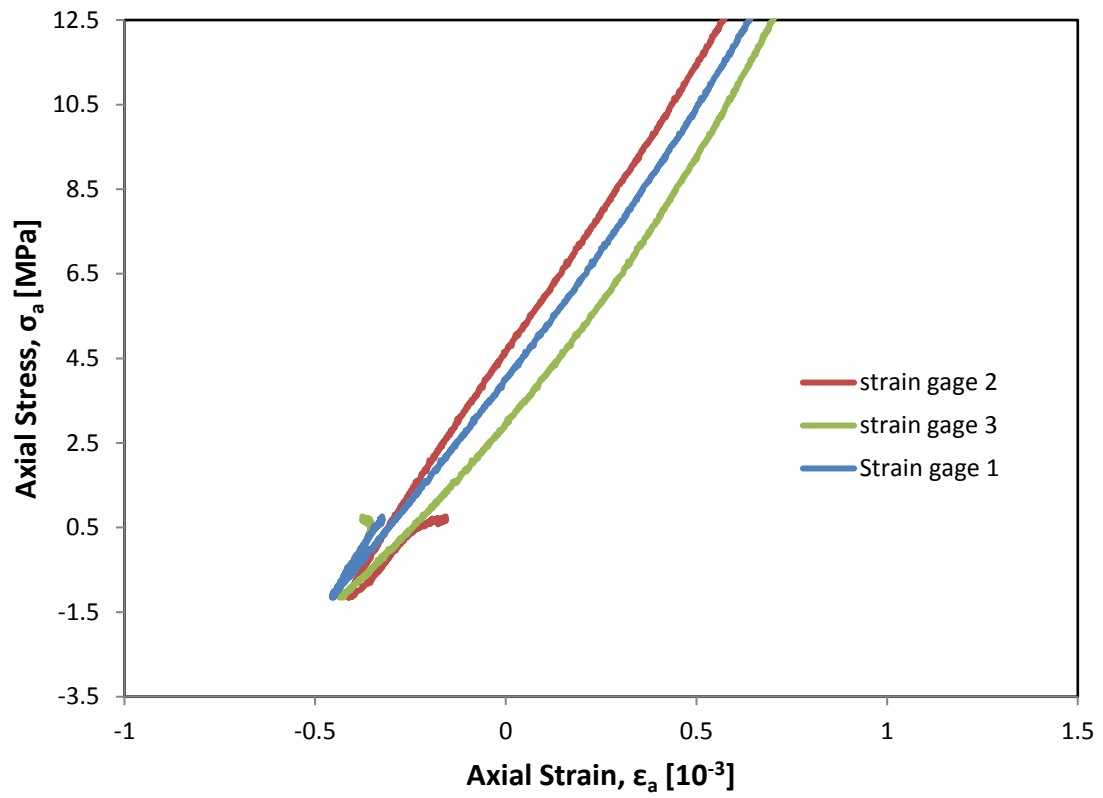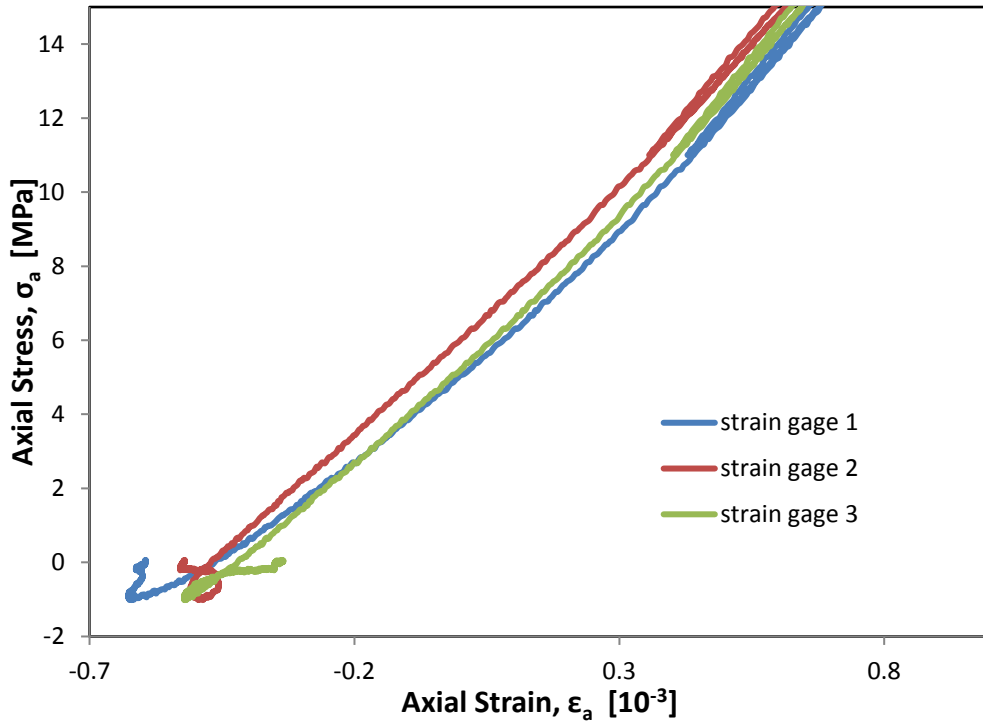| Test	Young's Modulus, E [GPa]
1	1.7
2	2.8
3	2.5
4	2.1
Average	**2.3**
Standard Deviation	**0.5**

Appendix B – Dog-bone Extension Stress-Strain

Figure 44. Stress-strain curves for specimen DB2 under 10 MPa confining pressure.

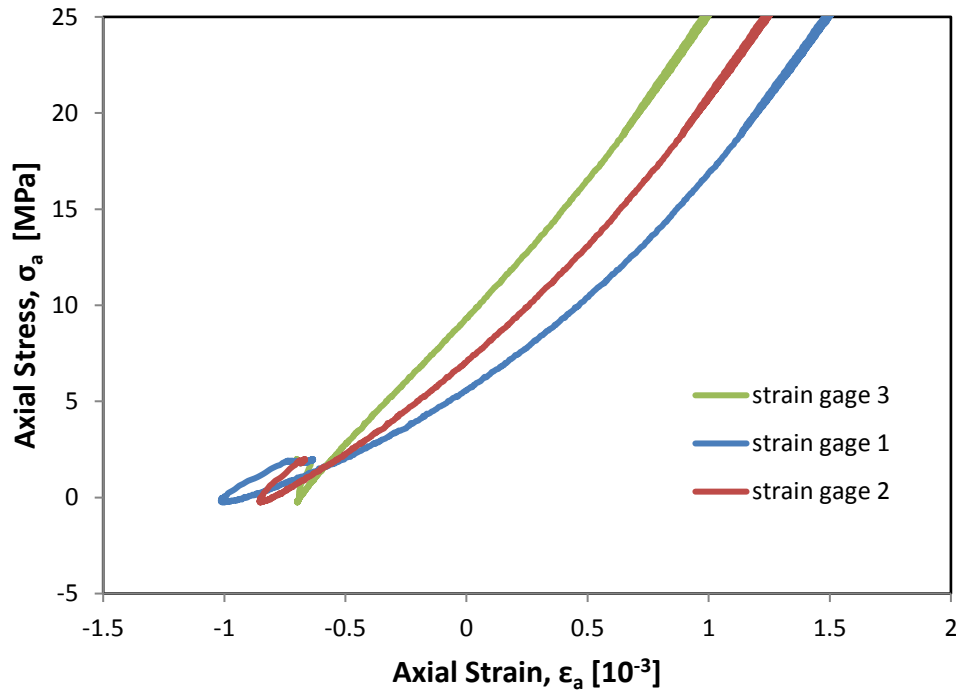Figure 45. Stress-strain curves for specimen DB3 under 15 MPa confining pressure.

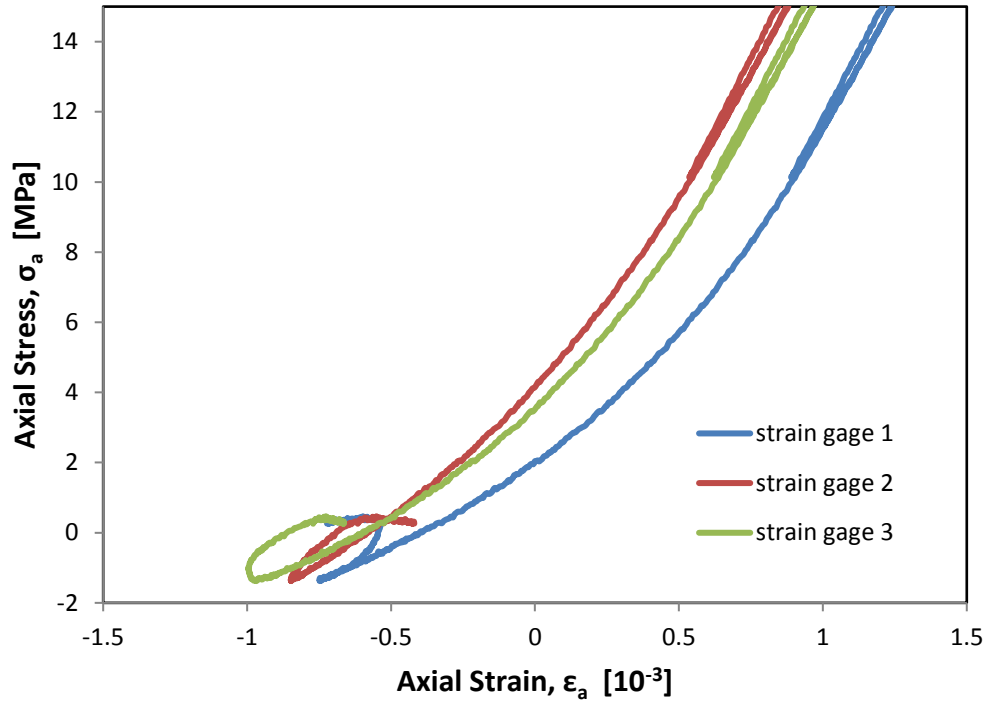Figure 46. Stress-strain curves for specimen DB6 under 25 MPa confining pressure.

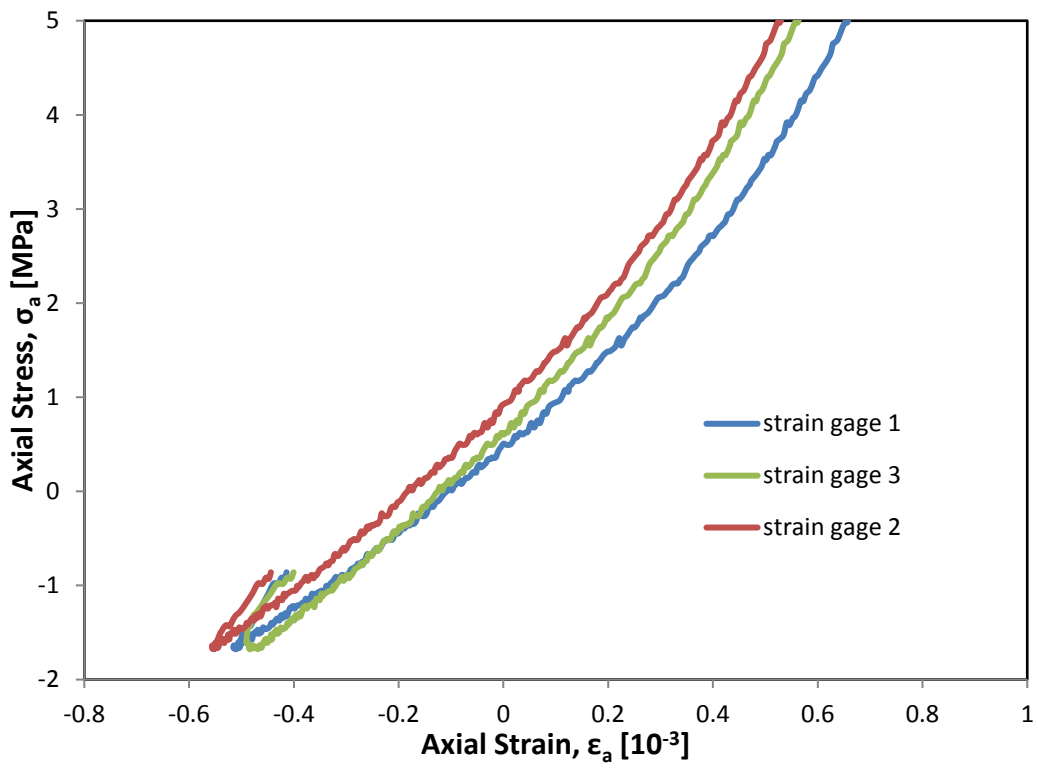Figure 47. Stress-strain curves for specimen DB7 under 15 MPa confining pressure.

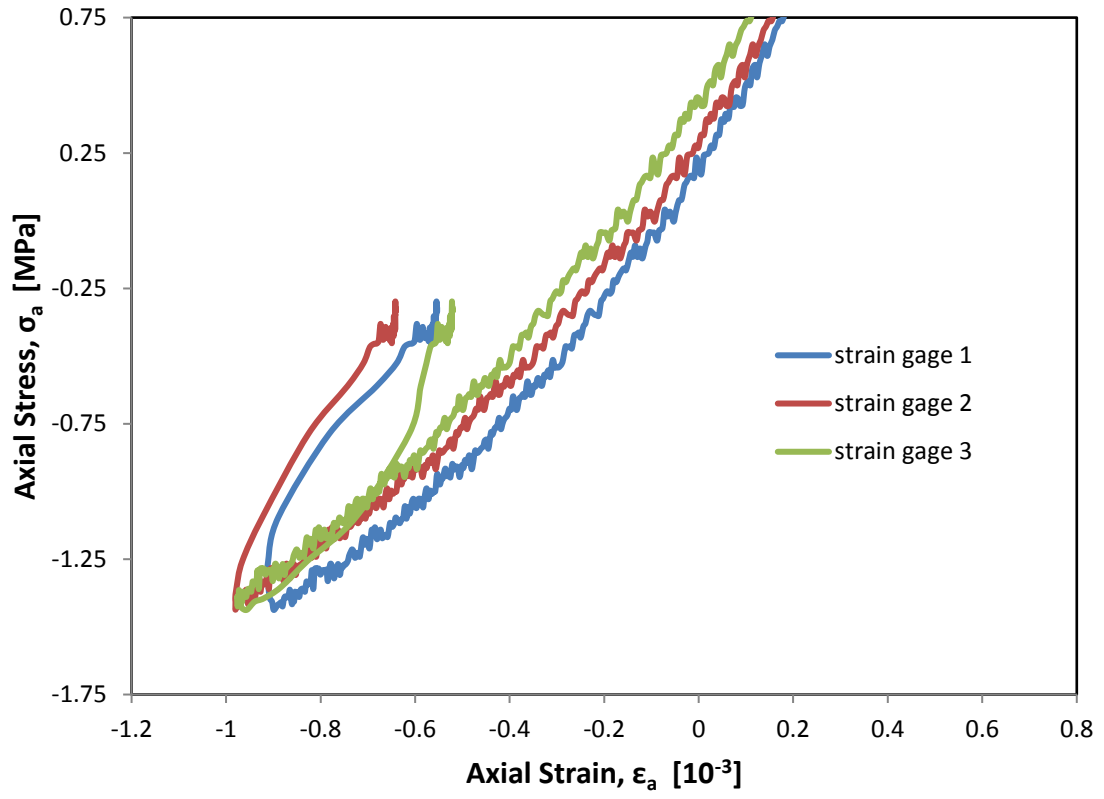Figure 48. Stress-strain curves for specimen DB8 under 5 MPa confining pressure.

Figure 49. Stress-strain curves for specimen DB12 under 0.75 MPa confining pressure.